MDPI

Article

Simulation on the Separation of Breast Cancer Cells within a Dual-Patterned End Microfluidic Device

Diganta Dutta [1,*], Xavier Palmer [2], Jung Yul Lim [3] and Surabhi Chandra [4]

[1] Department of Physics, Astronomy, and Engineering, University of Nebraska at Kearney, Kearney, NE 68849, USA
[2] Biomedical Engineering Institute, Old Dominion University, Norfolk, VA 23529, USA
[3] Department of Mechanical and Materials Engineering, University of Nebraska at Lincoln, Lincoln, NE 68588, USA
[4] Department of Biology, University of Nebraska at Kearney, Kearney, NE 68849, USA
* Correspondence: duttad2@unk.edu

Abstract: Microfluidic devices have long been useful for both the modeling and diagnostics of numerous diseases. In the past 20 years, they have been increasingly adopted for helping to study those in the family of breast cancer through characterizing breast cancer cells and advancing treatment research in portable and replicable formats. This paper adds to the body of work concerning cancer-focused microfluidics by proposing a simulation of a hypothetical bi-ended three-pronged device with a single channel and 16 electrodes with 8 pairs under different voltage and frequency regimes using COMSOL. Further, a study was conducted to examine the frequencies most effective for ACEO to separate cancer cells and accompanying particles. The study revealed that the frequency of EF has a more significant impact on the separation of particles than the inlet velocity. Inlet velocity variations while holding the frequency of EF constant resulted in a consistent trend showing a direct proportionality between inlet velocity and net velocity. These findings suggest that optimizing the frequency of EF could lead to more effective particle separation and targeted therapeutic interventions for breast cancer. This study hopefully will help to create targeted therapeutic interventions by bridging the disparity between in vitro and in vivo models.

Keywords: dielectrophoresis (DEP); alternating current electroosmosis (ACEO); microfluidic

1. Introduction

Microfluidics is a scientific field concerned with miniature fluid manipulation and the practices of microfluidics benefit a wide range of scientific applications, from biosensing to genome analysis to electrochemistry to environment monitoring, and more [1–5]. Microfluidic platforms offer precise control over fluid flow, cell manipulation, and biochemical reactions, allowing us to mimic aspects of the complex microenvironment of breast tumors and study cellular behaviors in a controlled setting [6–11]. Passive and active techniques are both utilized in microfluidics. Passive techniques include flow manipulation achieved solely from components that do not require energy—such as physical mesh filters, obstacles impeding flow, or grooves and trenches spatially interacting with the fluid. Active filtration requires mechanisms that actively work; this form of filtration is more functional but is more expensive to produce and maintain. Much research today regarding microfluidics considers such active techniques and has been spoken of at length by other authors [12–21]. One technique utilized in microfluidics is electroosmotic flow (EOF) or electroosmosis, in which flow is driven using an electric field and solutions doped with particles that will be affected by said EF. These particles are usually ions or dielectrics that move according to Coulomb's law. The motion of these particles then drives a bulk fluid flow. Alternating current electroosmosis (ACEO) is a type of induced-charge electroosmosis in which a non-uniform electric field provides a tangential force that affects the motion of ions to

control flow. This study will examine the range of frequencies most effective for ACEO to separate chosen particles. The frequency refers to how quickly the current changes polarity over time. Higher frequencies will result in more rapid changes in the electric double layer (EDL) on which the EOF depends. Furthermore, a time-dependent EOF can also affect fluid flow because, in different instances, the AC will be at different points in its cycle.

The set-up of a microfluidic experiment can include mechanical pumping in parallel with EOF within a tiny chip shaped with channels and fitted with electrodes. The bulk movement can be provided by pressure. However, precise adjustments come easier when using EOF. Our solution is doped with ions that provide Newtonian force to the surrounding fluid from their coulombic-driven motion required from the present EF. The charged surface of the electrodes creates an electrical double layer, a phenomenon driven by the chemical interactions of ions and the charged surface material in an aqueous solution. When this first layer is formed, known as the stern layer, other ions are further attracted according to Coulomb's law. Ions are attracted via the coulomb force screen in the first layer but are loosely attached and, therefore, more capable of influencing flow. However, because we use electrodes with an alternating current, the stern layer is also dynamic and thus influences the effects of electroosmosis and electrophoresis. Electrophoresis is the movement of ions or dielectrics in a uniform EF, such as direct current electroosmosis (DCEO). Dielectrophoresis, however, is concerned with the effect of non-uniform electric fields on ions and dielectrics, as in ACEO. Because of the non-uniform EF, ions are more dynamic than particles in DCEO. This increase in mutability makes ACEO ideal for mixing fluids. However, this mixing occurs on a micro-scale more suitable for research and analysis. Areas that utilize this technique include the following: lab-on-a-chip systems that enable fast and inexpensive mixing for analysis such as chemical and biological assays; drug delivery systems that take advantage of micromixing to ensure a homogenous solution for increased effectiveness; and chemical synthesis that requires precision when dealing with reactants; ACEO can provide better control over reaction conditions and results. Objects for mixing and transport within this experiment included chosen particles and cancer cell lines. Relevant to the concern of application towards cancer breast diagnostics, an insight was taken within the literature and the breast cancer cell lines, MD-MBA-231 and MCF-7, were selected for modeling, representing different cancers [6,22–24]. These were parameterized and added to the microfluidic device simulation.

In this study, our microchip includes three bands on either end that lead to a central chamber. The electrodes are placed throughout the channel, alternating from the top to the bottom of the chamber walls. The periodic placement of the electrodes is ideal for driving flow because they are placed so as not to counteract each other's EF, thus interfering with the desired motion. Without pressure-driven flow, the electrodes only contribute enough to exhibit vortical particle movement corresponding to each pair of electrodes. The pair of electrodes plays a crucial role in creating a non-uniform EF as they have opposite polarities: one is a cathode, while the other is an anode. In sum, we are utilizing microfluidics to simulate and optimize the process of generating improved diagnostic and therapeutic discovery devices for breast cancer. Towards this end, within this paper, we emphasize that this work entails a set of simulations that ultimately will require physical validation through physical paired tests. Already, prior work has emphasized the importance of predicting cell trajectories and orientation in microdevices [25–27]. Further, this work is not intended as a manufacturing aid and thus analyses of cost-effectiveness are beyond the scope of this work. Until then, this work functions as a theoretical aid towards improved cell separation to aid work in the microfluidic management of cell characterization and separation. Ultimately, our objective is to leverage microfluidic-based simulation approaches that can assist the development of improved diagnostic devices that can revolutionize breast cancer cell diagnostics.

2. Materials and Methods

2.1. Mathematical Method

Dielectrophoresis (DEP) is central to the working and understanding of this work; it is a technique that involves manipulating and separating particles in non-uniform electric fields based on their dielectric properties [28,29]. This technique attracts particles with positive DEP to high electric field regions and repels particles with negative DEP to weak electric field regions [28,29]. The Clausius–Mossotti (CM) factor plays a crucial role in understanding the behavior of particles in non-uniform electric fields [28,29]. It determines the polarity and magnitude of the induced dipole moment in the particle and influences its frequency-dependent behavior [28,29]. The imaginary part of the CM factor is associated with the loss during the polarization process. Dielectrophoresis is a versatile technique with numerous applications in various fields, such as biological research, environmental monitoring, and chemical analysis [28,29]. Its non-invasive nature makes it ideal for manipulating delicate biological specimens without causing damage or altering their intrinsic properties [28,29]. By exploiting differences in polarizability, DEP enables the selective manipulation of particles within a complex mixture, opening up new avenues for rapid and efficient particle sorting and separation [28,29]. The zero-polarization condition is an essential characteristic of DEP that has critical applications in determining particle dielectric properties and facilitating particle separation in mixtures [28,29]. It represents a unique opportunity for researchers to probe particles' dielectric properties and suspending media with unparalleled precision [28,29]. By precisely controlling the frequency of the applied electric field, researchers can exploit the zero-polarization condition to manipulate particles selectively based on their inherent dielectric properties [28,29].

This capability holds immense potential for applications requiring the precise separation and characterization of particles in complex mixtures, such as biomedical diagnostics and environmental monitoring [28,29]. In summary, understanding the Clausius–Mossotti factor and zero-polarization condition is critical in manipulating and separating particles with precision in non-uniform electric fields [28,29]. By leveraging these principles, researchers can engineer novel microfluidic devices and analytical techniques with enhanced capabilities and performance for various industries, from biotechnology to materials science.

Governing Equations

DEP force can be written as [30].

$$F_{DEP} = 2\pi\varepsilon_m r^3 Re[f_{CM}] \cdot \nabla \left[\overrightarrow{E}_{rms} \right]^2 \tag{1}$$

F_{DEP} is dielectrophoretic force, ε_m is permittivity of the medium, r is the particle radius, E is electric field and $Re[f_{CM}]$ is the real part of the Clausius–Mossotti factor.

Fluid flow inside the microchannel is induced by the continuity and Navier–Stokes equations [1].

$$\rho_f \left(\frac{\partial \overrightarrow{V}}{\partial t} + \left(\overrightarrow{V} \cdot \nabla \right) \overrightarrow{V} \right) = -\nabla P + \mu \nabla^2 \overrightarrow{V} + \rho_e \overrightarrow{E} \tag{2}$$

$$\nabla \cdot \overrightarrow{V} = 0 \tag{3}$$

V is the velocity of the fluid flow; p is the pressure and F represents the body force.

$$-\varepsilon_f \nabla^2 \phi = F(c_1 - c_2) \tag{4}$$

$$\nabla \cdot \left(\overrightarrow{V} c_i - D_i \nabla c_i - z_i \frac{D_i}{RT} F c_i \nabla \phi \right) = 0 \tag{5}$$

$$-\varepsilon_f \nabla^2 \psi = 0 \tag{6}$$

In this simulation, Poisson, Nernst–Planck and Laplace equations [31] are also used. F is the Faraday constant, R is the gas constant, T is the temperature, Zi is the valence, Di is the diffusivity, Ci is the ionic concentration, ε_f is the permittivity of the solution and ϕ is the electric potential.

Table 1 shows particles and breast cancer cells parameters. Two different types of cells are used in this simulation. These cells are early stage breast cancer cells (MCF7) and late-stage breast cancer cells (MDA-MB-231). Particles and cells diameter [32], relative permittivity and conductivity are given in Table 1.

Table 1. Particles and cells parameters.

Cell Name	Diameter (µm)	Conductivity (S/m)	Relative Permittivity
Particles	10	2.00×10^{-1}	40
MCF-7	11.2	2.50×10^{-1}	50
MDA-MB-231	12.4	3.10×10^{-1}	59

2.2. Schematic

Figure 1 shows our microchannel before applying a mesh. The length is 2650 micrometers (µm), and each crossroad on either end is 200 µm in height and width. Sixteen electrodes (eight pairs of positive and negative) are placed strategically to provide the electric field that is inherent in the DEP phenomenon. The electrodes are placed asymmetrically and are only placed inside the main channel, i.e., there is no voltage difference at the inlets or outlets. Fluid velocity inside the channel was measured by changing the inlet velocity. Our schematic features three inlets and outlets because the purpose of these trials is to better understand the microfluidic separation that is possible with long-range ACEO.
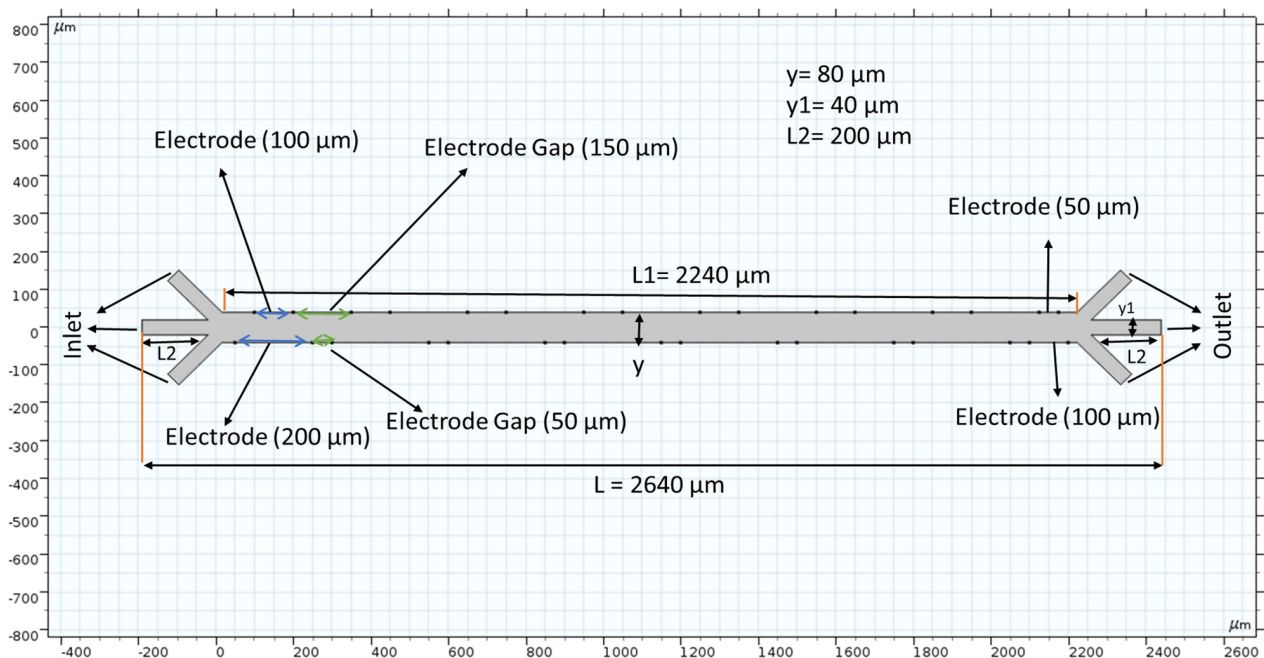

Figure 1. The microchannel schematic includes electrode placement. The scale of this channel is hundreds of microns wide and thousands of microns long. Electrode placement is asymmetric along the horizontal axis, and their spacing differs depending on which side of the channel is referred.

2.3. Boundary Conditions

The device's microchannel has three inlets and outlets. Each inlet used different inlet velocities and had atmosphere pressure assigned to the outlets. A no-slip boundary condition was used in the channel wall. The inertia term was not used in the Navier–Stoke

equation because of the low Reynolds number. In this study, Navier–Stoke and continuity equations were coupled, and both equations were solved using atmosphere pressure, velocity, and no-slip boundary conditions. Equation (3) is employed for electric potential. There are a total of 16 electrodes in the microchannel. Positive electrical potential (1 V) was applied in the top electrodes and negative electrical potential (-2 V) was applied in the bottom electrodes. We did not apply electric potential at the inlet and outlet boundary. For transport diluted species, there was no flux across the solid wall, and also the top and bottom inlet boundary. In the middle inlet boundary is used concentration (1 mol/m^3). In the outflow concentration c = 0 at the outlet boundary. For cell separation, a particle tracing module is used in this work. Drag force and dielectrophoretic force are coupled in this simulation. Particle tracing module also has 3 inlets and 3 outlets in the channel. Outlet boundary is used for freezing conditions. There was a bounce wall condition used for the particle tracing module. Three different types of cells are released in the bottom inlet boundary at the same time. The release time ranges from 0 to 15 s, and every time it released 1 particle. Inlet fluid velocity (200 μm/s) was applied to the top and bottom inlet boundary and 300 μm/s was applied in the middle inlet boundary to transport to the cells and particles. Equations (1) to (6) are solved using the above boundary conditions via COMSOL Multiphysics 5.3a.

2.4. Mesh

COMSOL provides a physics-controlled mesh to record the fluid velocity at many points. The element quality was skewed. The average element quality is 0.8327, the element area ratio is 0.01414, and the number of elements is 3836. This study uses 3323 triangles, 513 quads, 551 edge elements and 54 vertex elements. A total of 2451 mesh vertices were used in the entire geometry. Mesh generation was implemented in the simulation region. Figure 2 top shows grid independent study. Grid independence was assessed in this study. We evaluated average velocity at the middle of the channel through changing grid size. In this study, we used grid sizes 25, 20, 15, 10 and 5 μm. The average velocity was 49.78 nm/s when the grid size was 25 μm. At 20 μm grid size, we calculated average velocity to be 49.98 nm/s. The average velocity is almost constant when the grid size changes from 20 to 5 μm. We can conclude that our numerical results did not add errors from case to case as the velocity changed very little.
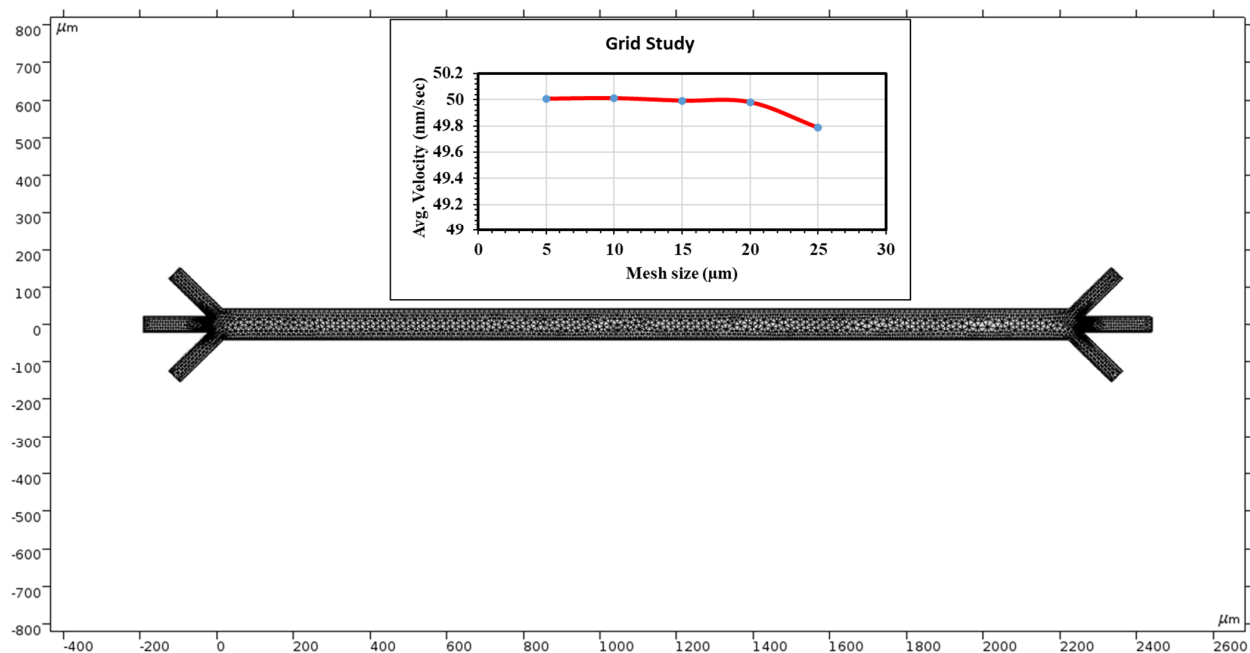

Figure 2. COMSOL Multiphysics application provides a mesh to measure velocities at many points along the chamber. The top graph shows a grid independent study.

2.5. AI-Use Acknowledgement

Grammarly AI was used to spell check, address grammar, add clarity, improve delivery, and re-organize portions that were already produced, to reconcile writing styles between authors and present a unified style.

3. Simulations and Results

3.1. Voltage Induced in the Microchannel

The alternating current induced through the electrodes creates a non-uniform electric field to manifest the dielectrophoresis phenomena throughout the channel. The surface graph of the voltage at 15 s recorded using our mesh is shown in Figure 3. Because the electromotive force (EF) provided alternates, the EF produced is periodic. The asymmetric placement of the electrodes amplifies the non-uniformity of our EF. The voltage is crucial for electroosmosis, and the AC EMF introduces dielectrophoresis commonly used for micro mixing and administration. Because of the small scale, the voltage readings are shown by the legend on the left of Figure 3. The applied voltage is 1 V in the top electrodes and −2 V in the bottom electrodes. The color bar on the left side of Figure 3 represents the surface potential (V) inside the channel.
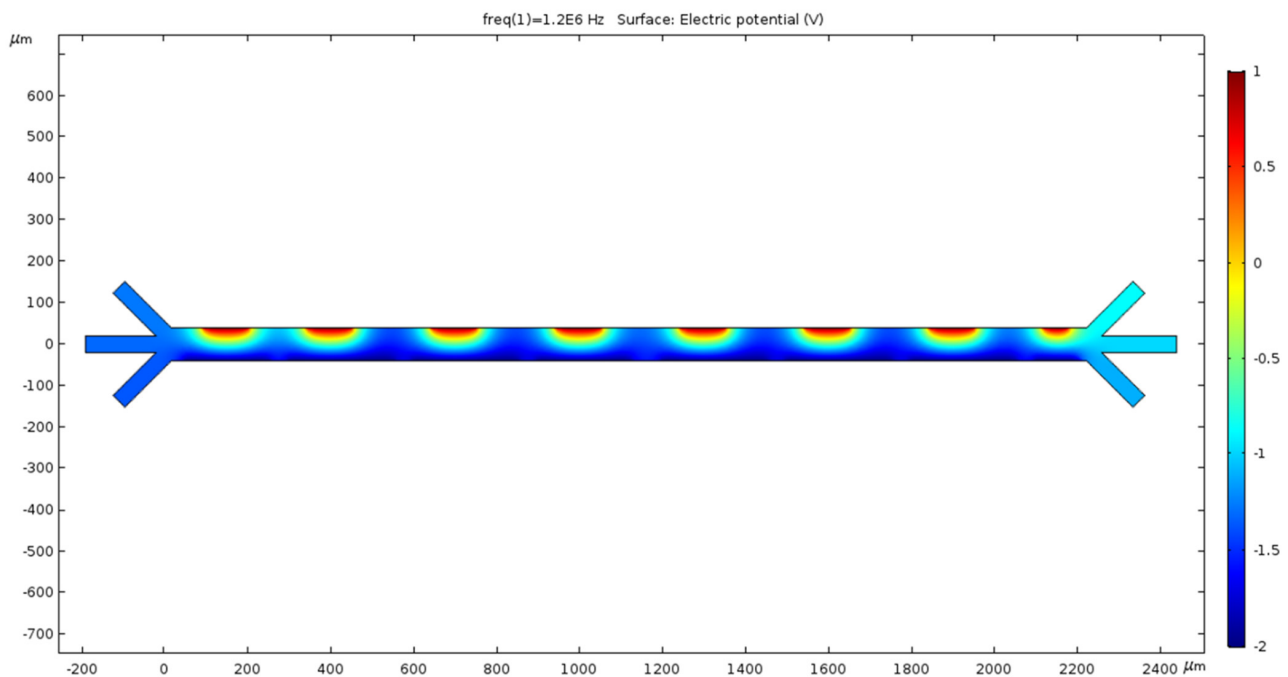

Figure 3. The microchannel exhibits a surface graph showing the electric field's magnitude in various locations throughout the chamber. Color represents the extremities of the voltage on a micro scale.

3.2. Microchannel Fluid Velocities Trialed

3.2.1. 0 nm/s

In the absence of an inlet pressure, the ACEO phenomenon produces fluid velocity. The flow is shown to have a vortical motion pattern centered between the electrode locations. Hydrodynamic force was absent in this condition and hence no fluid flow was noticed at the outlets. To generate the ACEO fluid flow, we applied the frequency (1200 kHz) to the electrodes; at the top electrodes and bottom electrodes the applied voltages were 1 V and −2 V, respectively. The color bar on the left side of Figure 4 represents the velocity magnitude (m/s) inside the channel.

3.2.2. Trial of 50 nm/s Fluid Velocity

The microchannel simulated with an inlet velocity of 50 nm/s now has a net flow. The surface view of the velocity magnitude shows a sinusoidal fluid motion pattern

corresponding to our electrode placement. Every peak of the sin wave pairs with the low-voltage spots are shown in Figure 3. The outlet velocity is slower than the inlet because of the color difference in Figure 5. The hydrodynamic force was present in this condition, and we observed fluid flow patterns inside the channel. To generate the ACEO fluid flow, we applied voltage and frequency (1200 kHz) to electrodes. The color bar on the left side of Figure 5 represents the velocity magnitude (m/s) inside the channel.
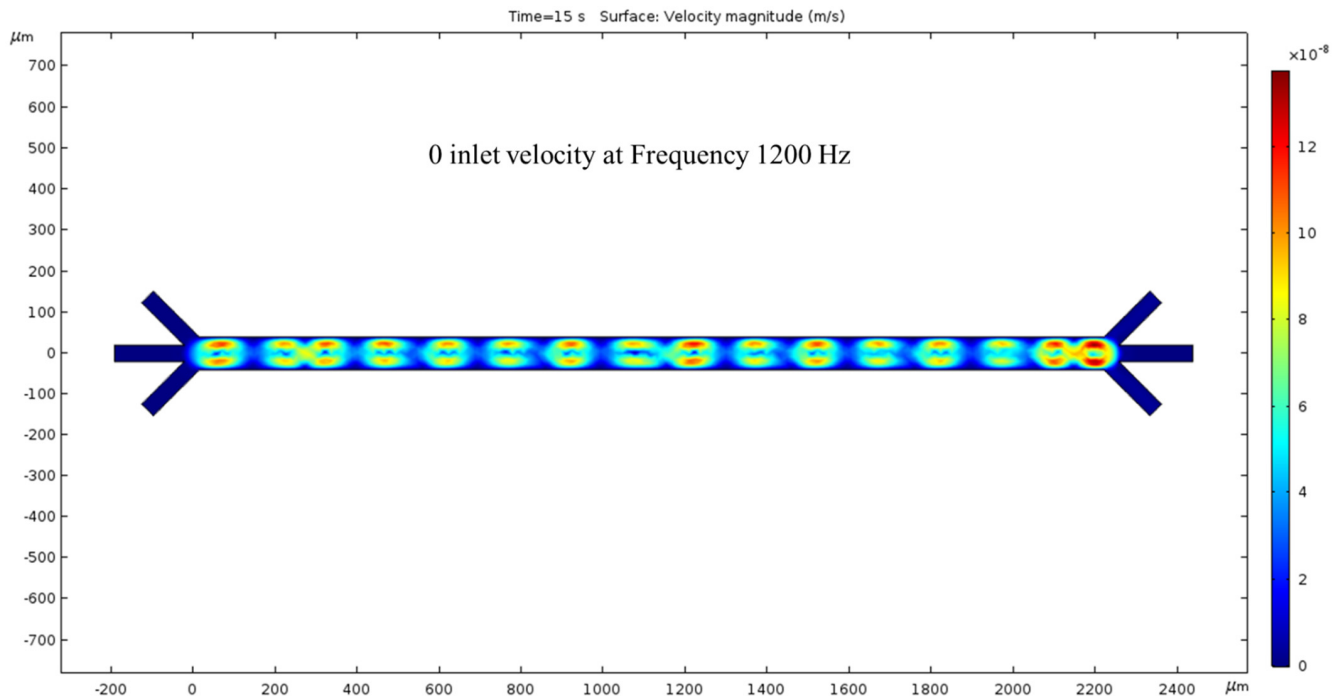
Figure 4. While the inlet velocity remains zero, a surface view of the fluid velocity, taken at the 15 s mark, depicts vortical motion corresponding to the 1200 kHz AC applied to the electrodes.
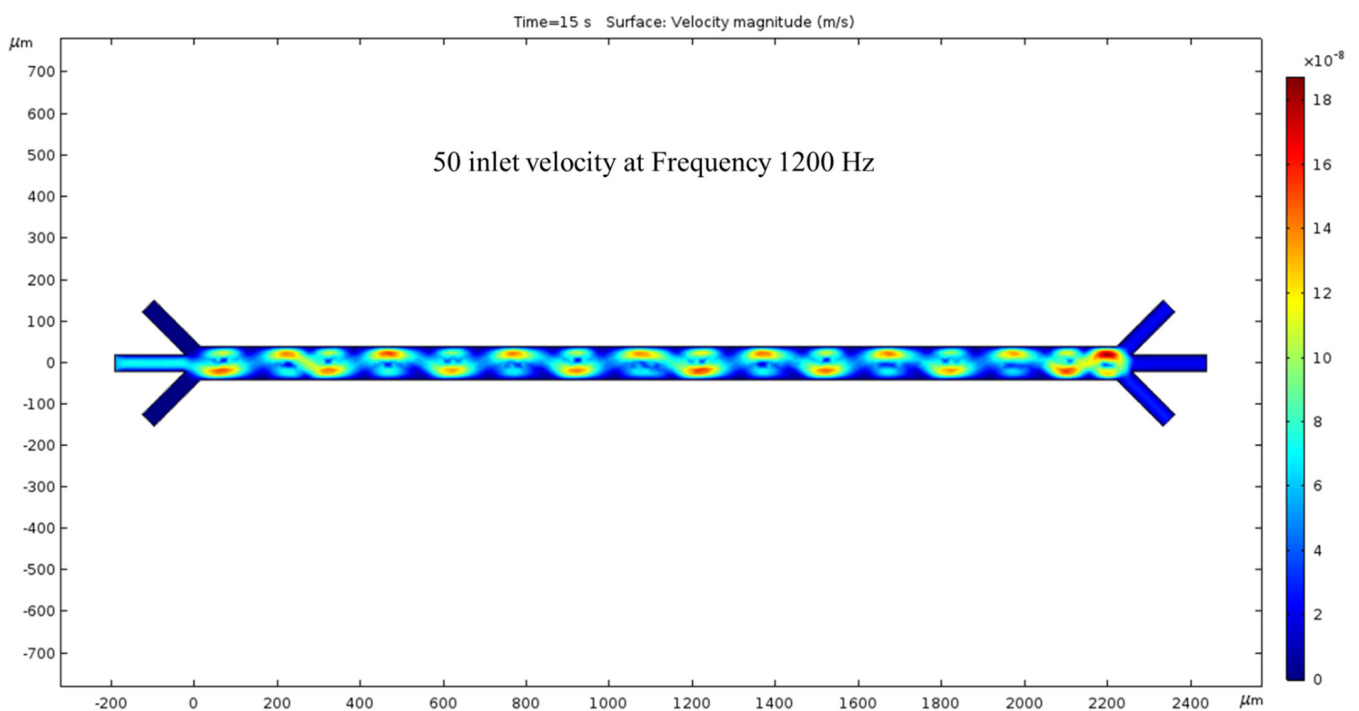
Figure 5. The surface graph of the velocity at 15 s with a 50 nm/s inlet velocity and 1200 kHz AC exerted on the electrodes.

3.2.3. Trial of 100 nm/s Fluid Velocity

The inlet velocity is increased again by 50 nm/s to 100 nm/s. At 15 s, the velocity has increased compared to Figure 5. The crests and troughs of the sin wave are redder than the previous figure, and the trail's color is also more prominent. As expected, the inlet velocity is lower than the outlet velocity, and their difference is proportional to the previous inlet/outlet velocity difference. By further increasing the inlet velocity, we expect the outlet velocity to increase. In this condition, both the hydrodynamics force and ACEO phenomenon play a noticeable role for fluid flow inside the channel. To generate ACEO fluid flow, we applied voltage and frequency (1200 kHz) to electrodes. The color bar on the left side of Figure 6 represents the velocity magnitude (m/s) inside the channel.
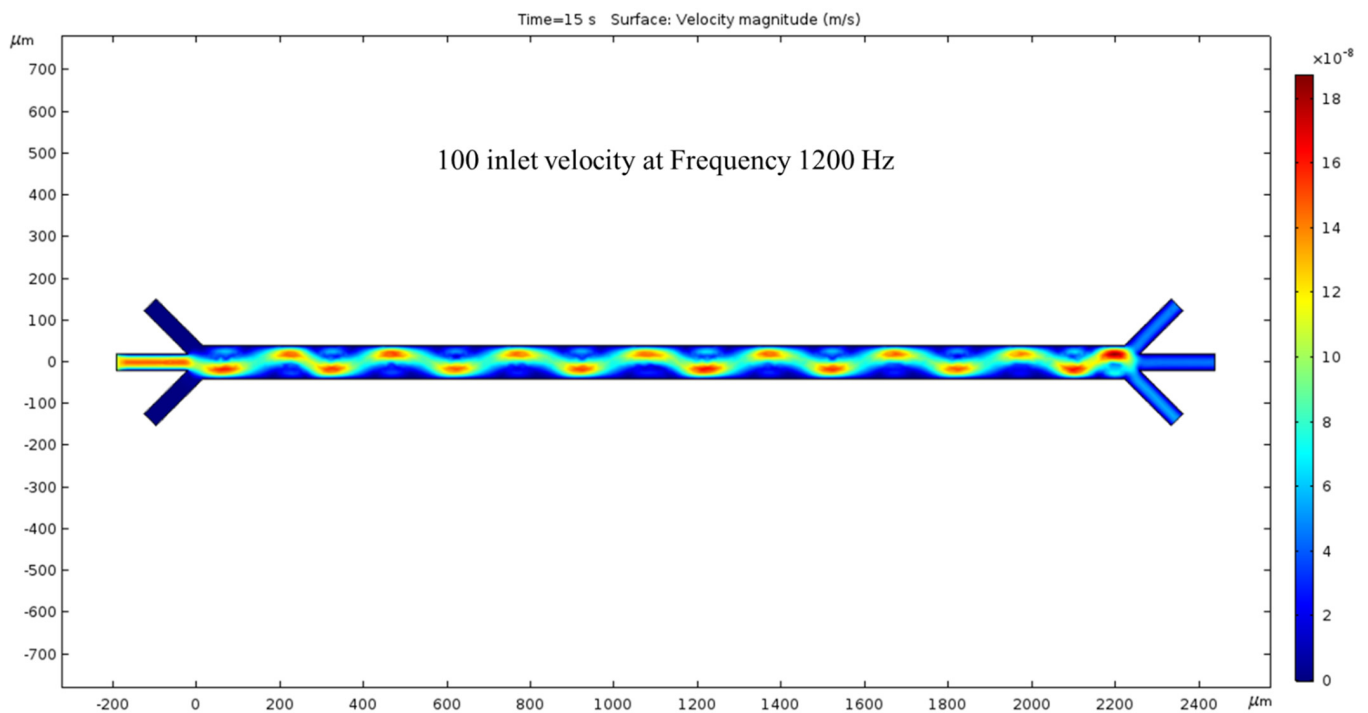

Figure 6. The surface graph of velocity at 15 s with a 100 nm/s inlet velocity and 1200 Hz AC exerted on the electrodes.

200 nm/s—The fourth time we ran the simulation, the inlet velocity was increased by 100 nm/s, giving a total of 200 nm/s inlet velocity. The fluid motion was faster, as shown by the intense-colored sin wave. The colors have changed again, and the previous trials sin wave is now greener with peaks and troughs that are not as red but more yellow. In other words, once we increase the inlet velocity to 200 nm/s, the magnitude of the velocity of the fluid decreases at the location of the wave's extremes compared to Figure 6. The difference between the velocity magnitude of the inlet vs. the outlet is consistent with the previous trials, as the red inlet contrasts with the blue outlet. In this condition, the hydrodynamic force was dominated by the fluid flow, but the ACEO force was negligible compared to the hydrodynamics force. The color bar on the left side of Figure 7 represents the velocity magnitude (m/s) inside the channel.

Maximum Velocity vs. Time (0 nm/s)—Figure 8 shows the maximum velocity magnitude inside the microchannel. The 10 Hz trial (yellow) showed a gradual increase, peaking at the end of the trial. The values were recorded at 5, 10, and 15 s. The 10 Hz trial resulted in 8.34, 19.5, and 40.3 nm/s, respectively. The 100 Hz trial (royal blue) also increased over time and peaked at the end, but more rapidly than the 10 Hz trial. The respective values for the Hz trial are 5.32, 42.1, and 149. The 1000 Hz trial (green) peaked at 10 s and decreased for 5 s. Its values are 0.290, 84.3, and 24.5 nm/s. The 10 and 100 Hz trials matched trends, and the 1000 and 10,000 Hz trials also did. At 10,000 Hz, the extremity is less than the previous

trial. In contrast, increasing the frequency from our first to the second trial increased its maximum value. However, comparing the 1000 and 10,000 Hz trials, the extremity has less magnitude. The values at 5, 10, and 15 s for the largest frequency curve (navy blue) are 7.14, 27.8, and 25.3, respectively.
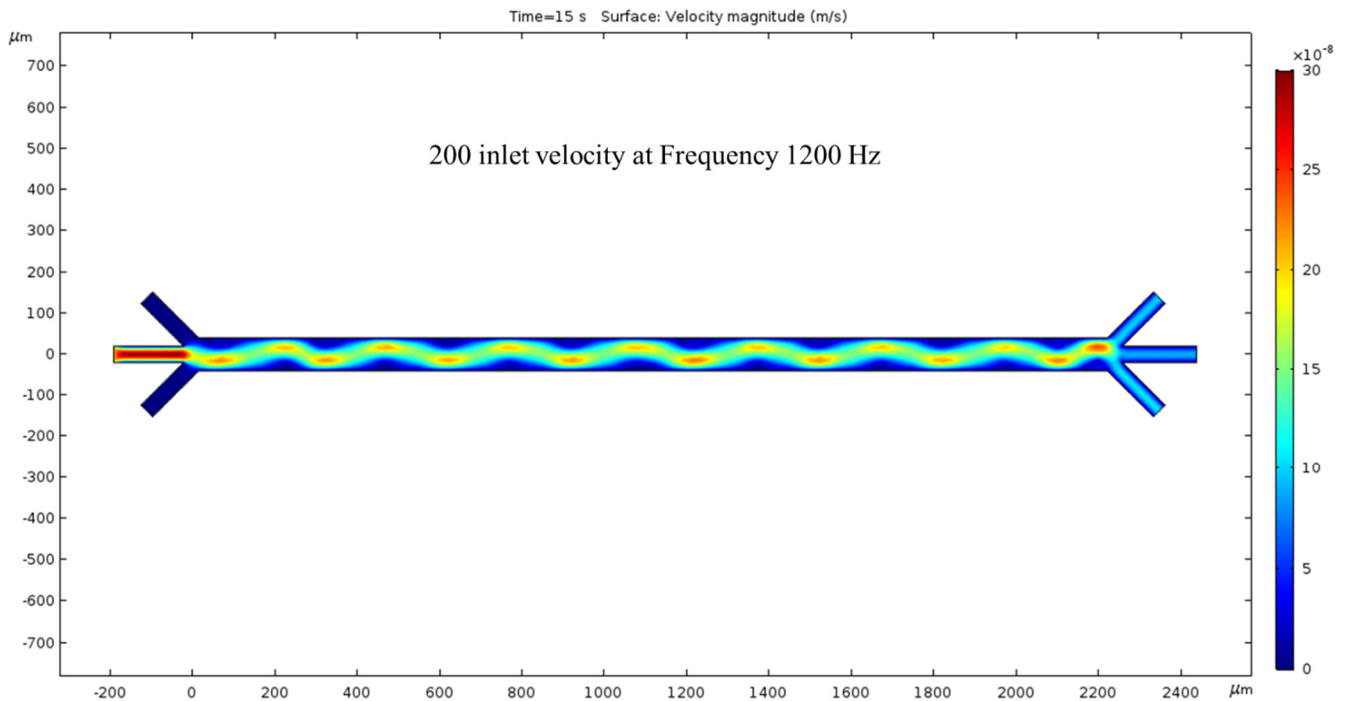

Figure 7. With 1200 kHz AC through the electrodes, at 15 s, a 200 nm/s inlet velocity results in a clearer surface view of the ACEO phenomena.
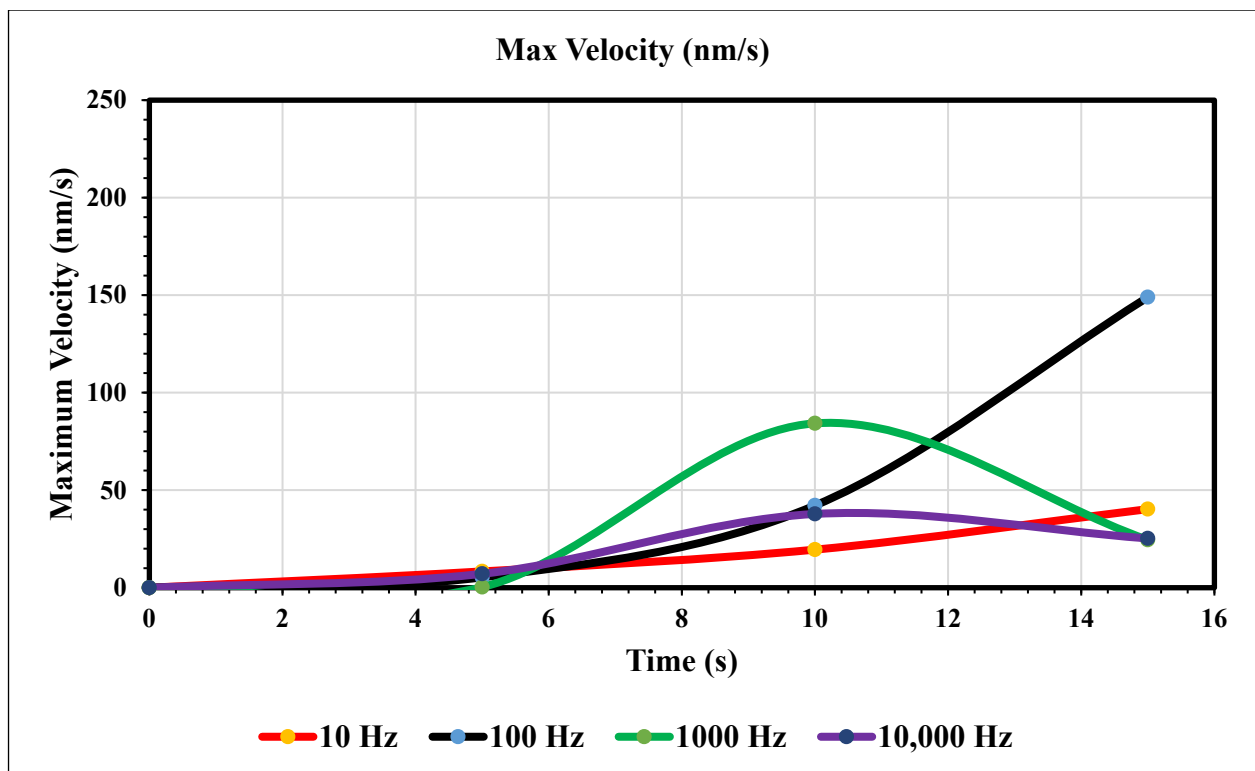

Figure 8. The graph of maximum velocity over 15 s when the inlet velocity is 0 nm/s.

Maximum Velocity vs. Time (50 nm/s)—Our simulation results (Figure 9) show different trends once the inlet velocity is increased to 50 nm/s. This graph shows peaks, the first being at 5 s for the 1000 Hz trial (green), and the second peak occurs at 10 s for the 10 Hz trial (yellow). The corresponding values for these extremities are 189 and 202 nm/s. After these peaks, the graph decreases back to 50. The 10 Hz curve lacks the time to increase again but based on the behavior of our 1000 Hz trial, we can assume its trend to be like that of the green curve. As for our royal and navy-blue curves (100 and 10,000 Hz), we see a peak at 15 s (184 nm/s) and a constant curve with no change, respectively.
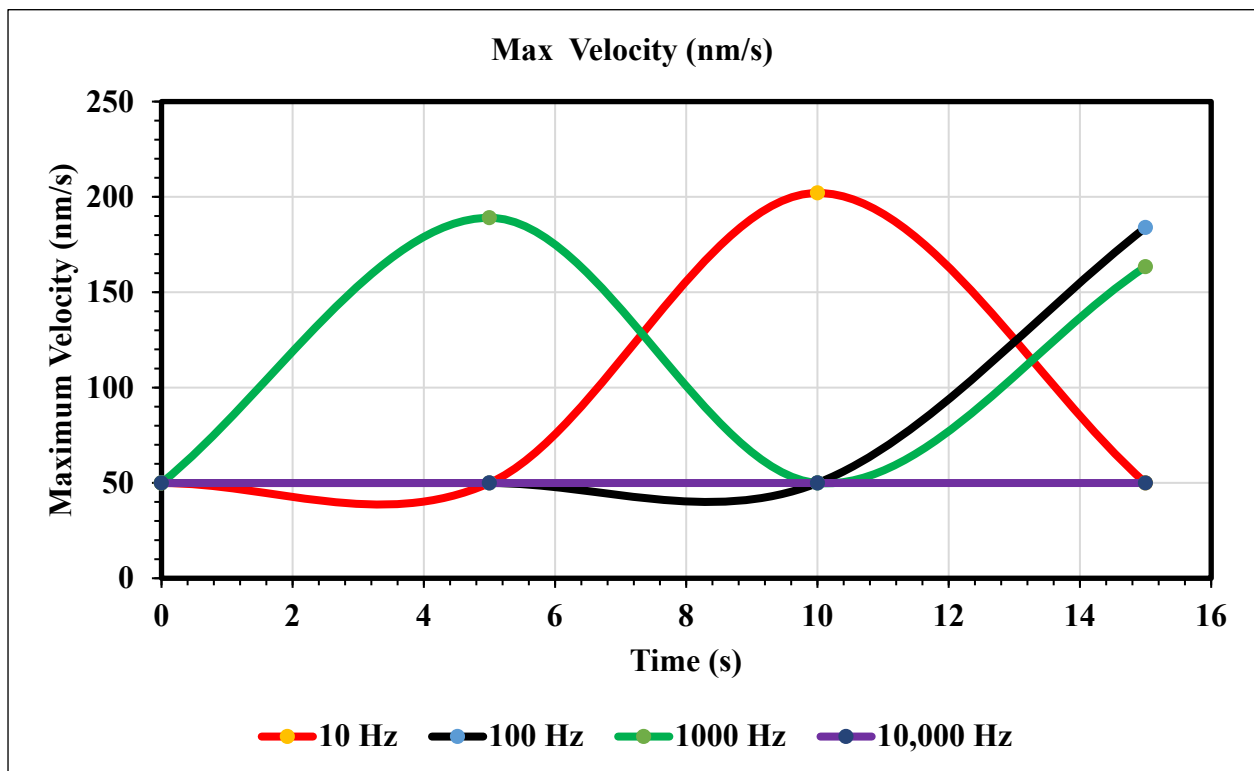

Figure 9. The maximum velocity graphed over 15 s using an inlet velocity of 50 nm/s.

Maximum Velocity vs. Time (100 nm/s)—Figure 10 shows the maximum velocity magnitude inside the microchannel. The maximum velocity for this graph only varies for the 10 and 1000 Hz trials. Figure 10 shows the peak max velocity occurring at 15 s with values of 135 and 136, respectively. Furthermore, when the inlet velocity is 100 nm/s, an AC of 100 and 10,000 Hz produces no change in fluid velocity.

Maximum Velocity vs. Time (200 nm/s)—Figure 11 shows the maximum velocity magnitude inside the microchannel. The inlet velocity is increased to 200 nm/s, and the 100 Hz trial is the only trial with a varying maximum velocity. At 10 s, the 100 Hz frequency trial peaks its maximum velocity at 211 nm/s. The rest of the trials remain constant for the full 15 s. However, note that if the domain was increased, we should not assume that these frequencies would remain constant because the maximum velocity only varies with time.

Figure 12 shows a graph of velocity in x direction vs. channel height. This study observed the parabolic velocity profile inside of the channel. The Navier–Stokes equation stabilized between the viscous force and pressure, hence there is a noted parabolic velocity profile. This work also observed zero velocity at the wall, as we applied a no-slip boundary condition at the wall. We found a maximum velocity when the height of the channel was between 20 µm and 30 µm. In this work, we measured the velocity profile in the middle of the channel by changing the inlet velocity. The velocity increased when the magnitude of the inlet velocity changed. Figure 12 represents the validation of our work, as we found the

parabolic velocity profile inside of the channel and magnitude of the velocity increased as the pressure changed.
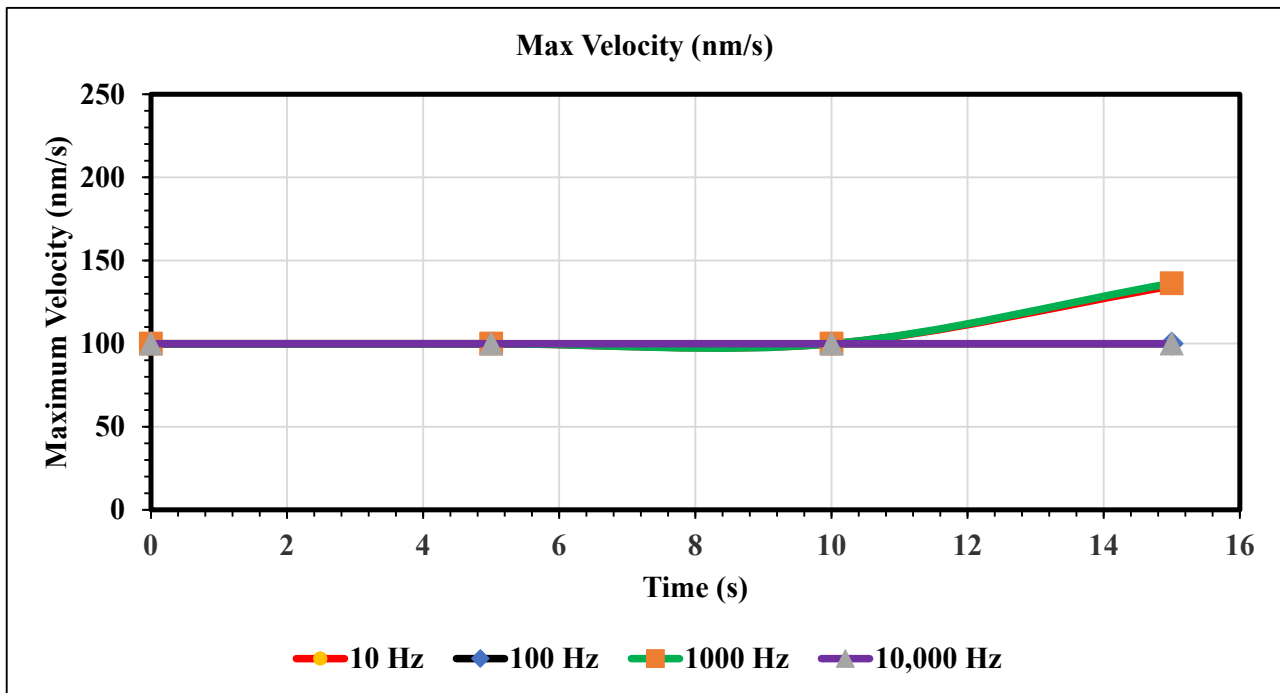

Figure 10. The following graph shows the maximum velocity for each simulation over the course of 15 s.
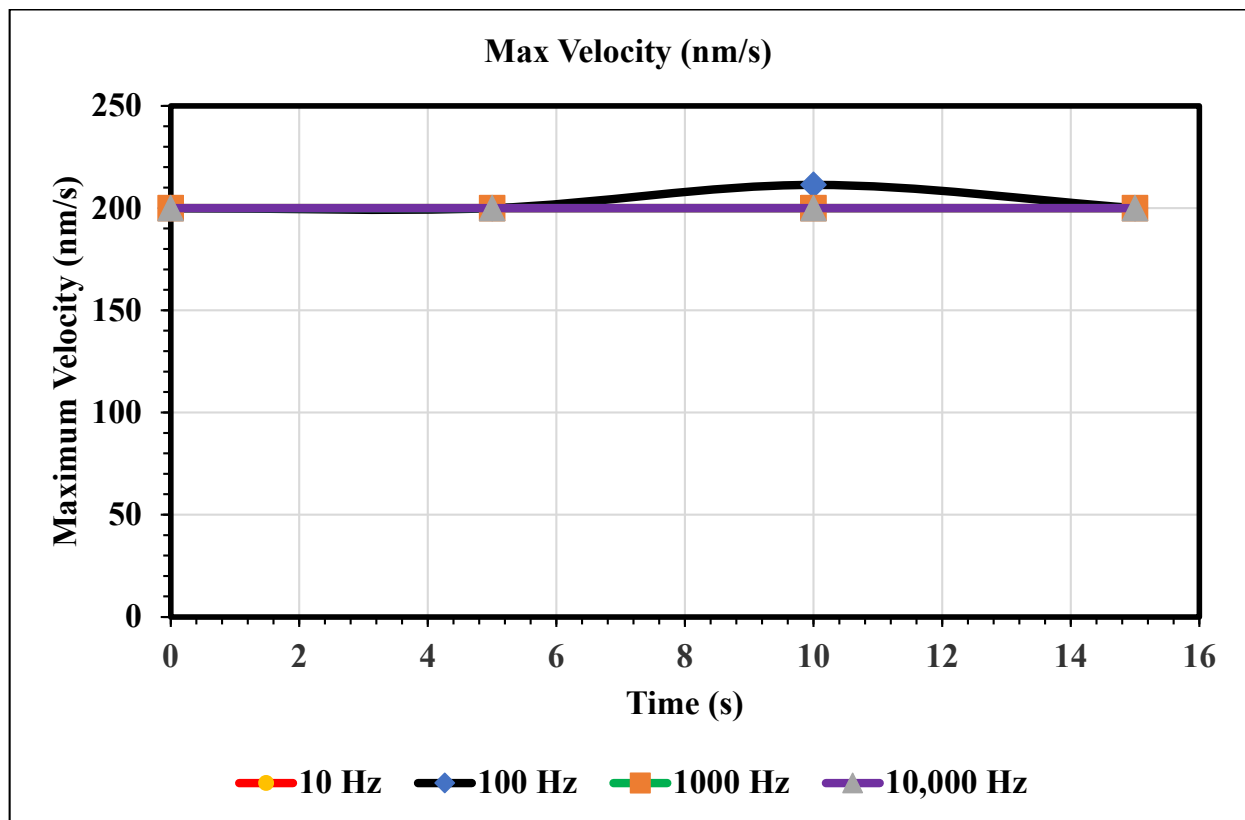

Figure 11. This graph shows the largest velocity recorded using our mesh for varying frequencies of AC over the domain of 0 to 15 s.
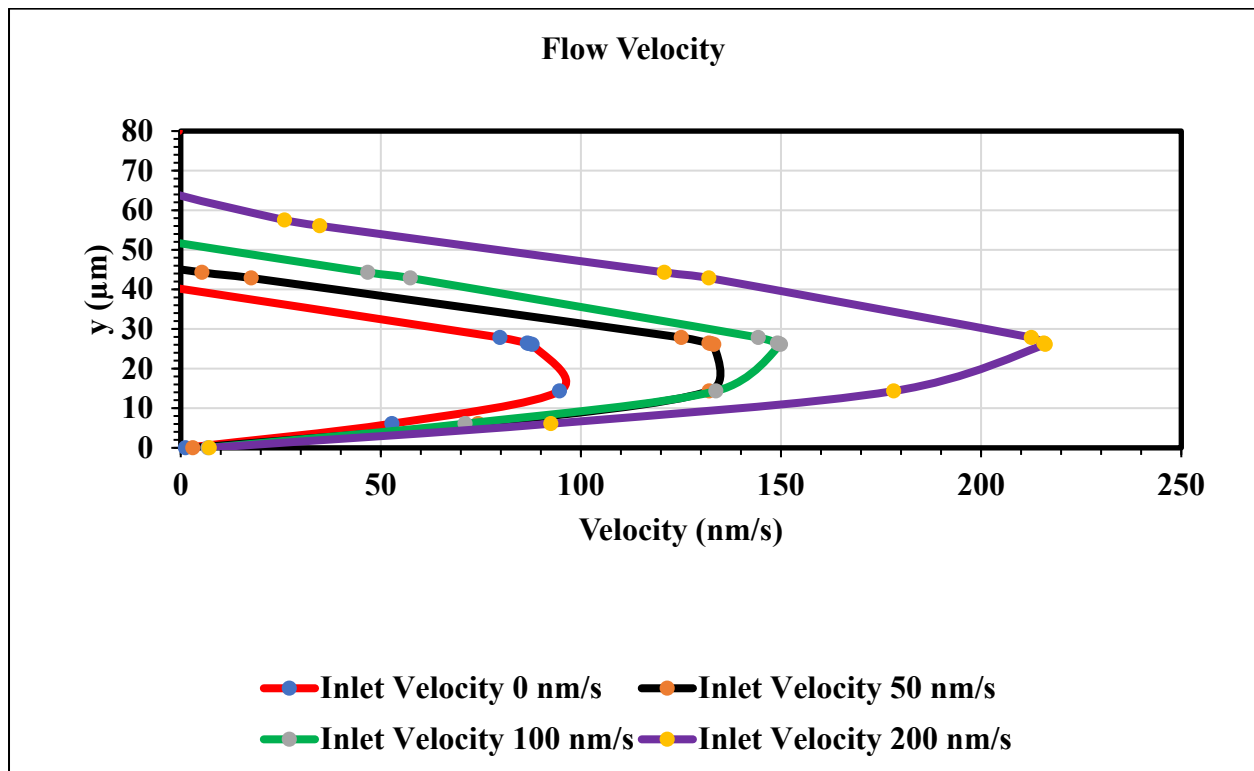
Figure 12. Velocity in x direction vs. the channel height (y) graph at the middle of the channel when time is 15 s.

Particle Trajectories (100 kHz)—Figure 13 shows particles and cells trajectories inside the microchannel at 100 kHz. We used particles and two different types of cells lines; in this work, these were early stage breast cancer cells (MCF7) and late-stage breast cancer cells (MDA-MB-231). Particles, MCF7 and MDA-MB-231 cells are shown as brown, blue and green colors, respectively. We applied 1 V electrical potential at the top electrodes and −2 V electrical potential at the bottom electrodes in all cases for cell and particle separation. To achieve the DEP phenomenon, we must increase the frequency by 1000-fold. So, our further observations will be in units of kHz starting at 100. When observing the electrokinetic phenomenon at 100 kHz, the particles and cells do not achieve any separation and they all exit through the bottom outlet. Furthermore, they are scrunched up, and their paths overlap.

Particle Trajectories (800 kHz)—Figure 14 shows particles and cells trajectories inside the microchannel at 800 kHz. When the frequency of the current through our electrodes increases to 800 kHz, we can notice a change in particles and cells trajectory. They are less overlapped, and we can infer a further separation of material types as we increase the frequency. The particles leave through the bottom outlet; the MCF7 and MDA-MB-231 cells are shown to exit in the middle outlet.

Particle Trajectories (1000 kHz)—Figure 15 shows particles and cells trajectories inside the microchannel at 1000 kHz. The frequency is increased to 1000 kHz to separate the particles and cells. In this depiction, the particles and cells have warped enough to no longer exit through the same outlet. Instead, the MCF7 and MDA-MB-231 cells are shown to exit through the middle outlet, while the particles still leave through the bottom outlet. The split of the MDA-MB-231 cells supports our assumption that segregation can be achieved if we increase the frequency, because our particles can be filtered.
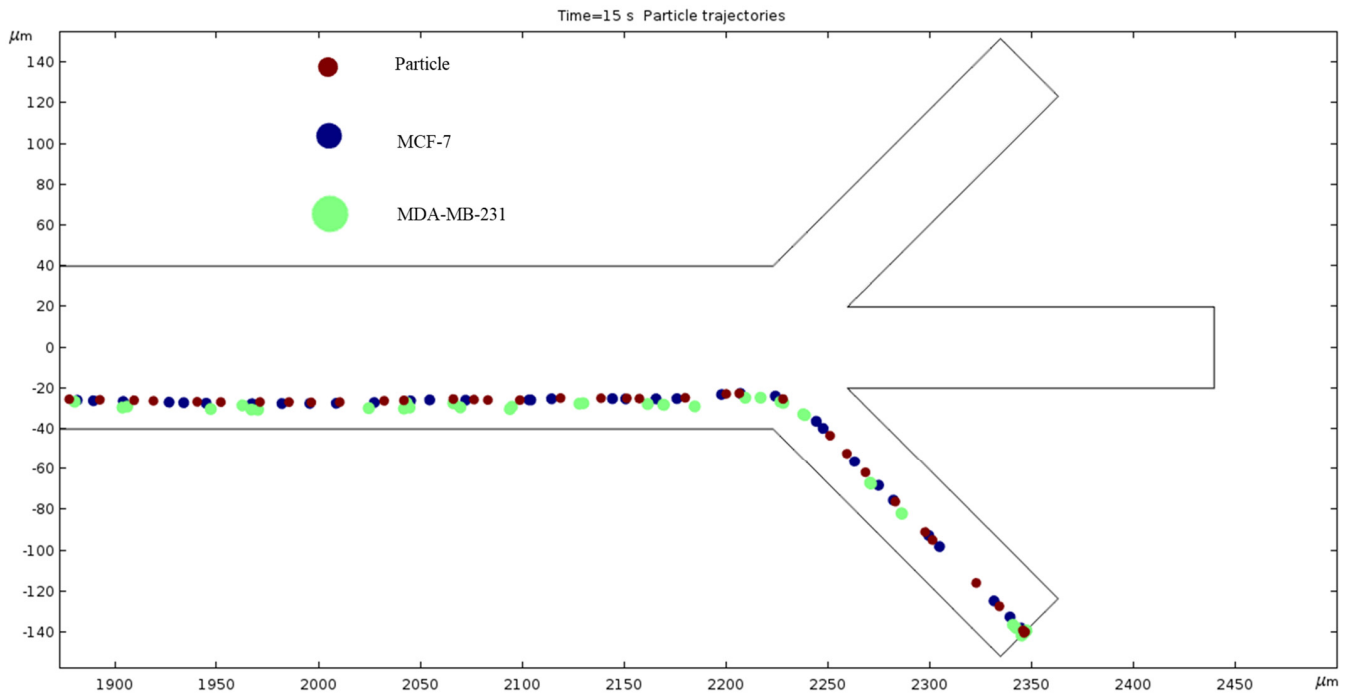
Figure 13. A diagram of a graph of particles and cell trajectories while the frequency of AC through the electrodes is 100 kHz.
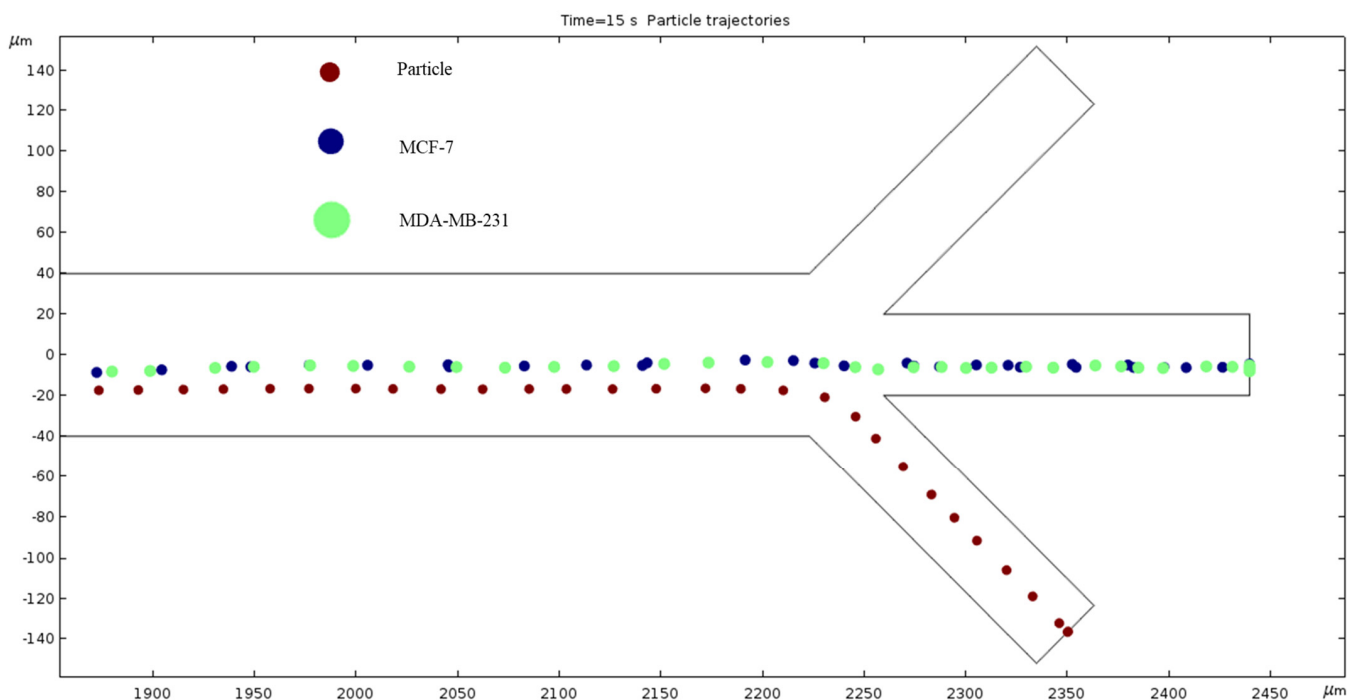

Figure 14. A diagram of a graph of cell trajectories while the frequency of AC through the electrodes is 800 kHz.

Particle Trajectories (1200 kHz)—Figure 16 shows particles and cells trajectories inside the microchannel at 1200 kHz. When the frequency is set to 1200 kHz, we can now see the separation of cells and particles at our microchannel outlet. The MDA-MB-231 cells flow out of the top outlet, the MCF 7 cells out of the middle outlet, and the particles flow out of the bottom outlet Figure 16 (Supplementary Video). Through this process, we can effectively filter the different particles and cells.
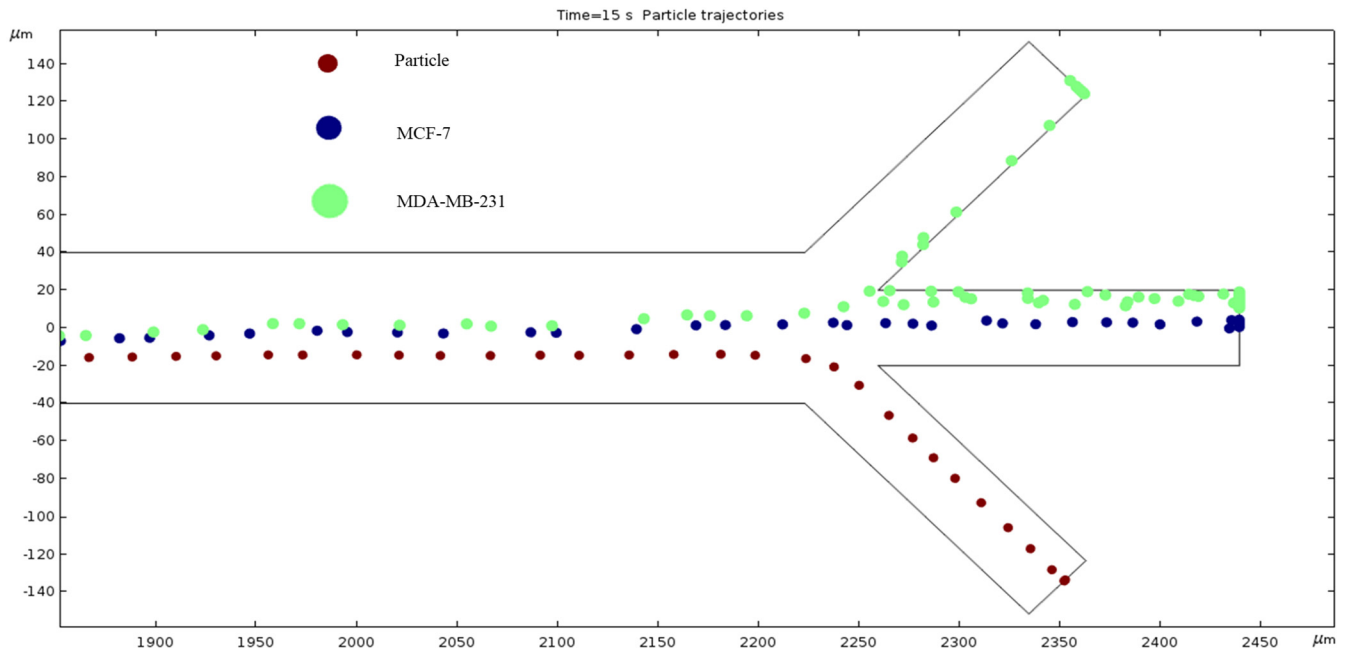
Figure 15. A diagram of the separation of particles due to the DEP phenomenon produced at 1000 kHz AC.
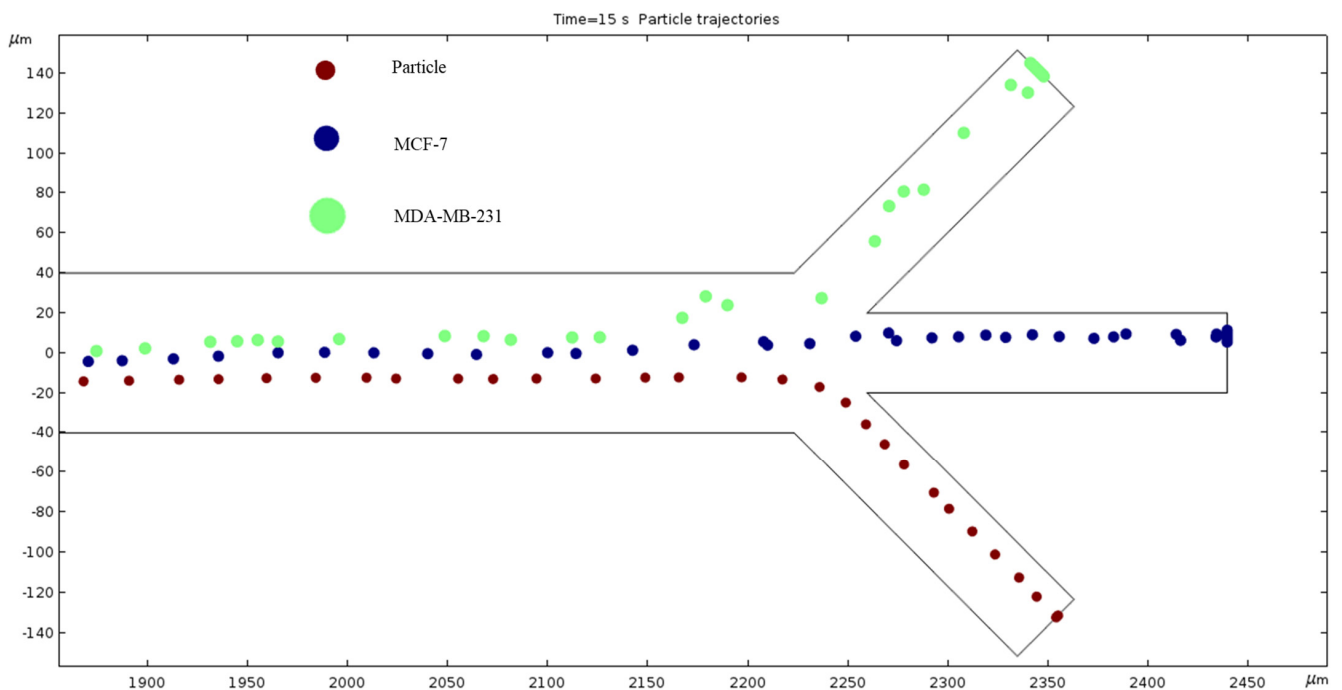

Figure 16. The depiction of our microchannel filtering different cells through DEP with a frequency of 1200 kHz.

Particle Trajectories (1500 kHz)—Figure 17 shows particles and cells trajectories inside the microchannel at 1500 kHz. The frequency is increased to 1500 kHz and our cells' motion path is changed. The trend seems to bend further counterclockwise, so the MDA-MB-231 cells no longer make it through the top outlet, and the MCF 7 cells have a similar path to the trajectory of the MDA-MB-231 cells in Figure 17. The particles still exit through the same outlet but are slightly closer to the upper edge of said outlet compared to Figure 17.
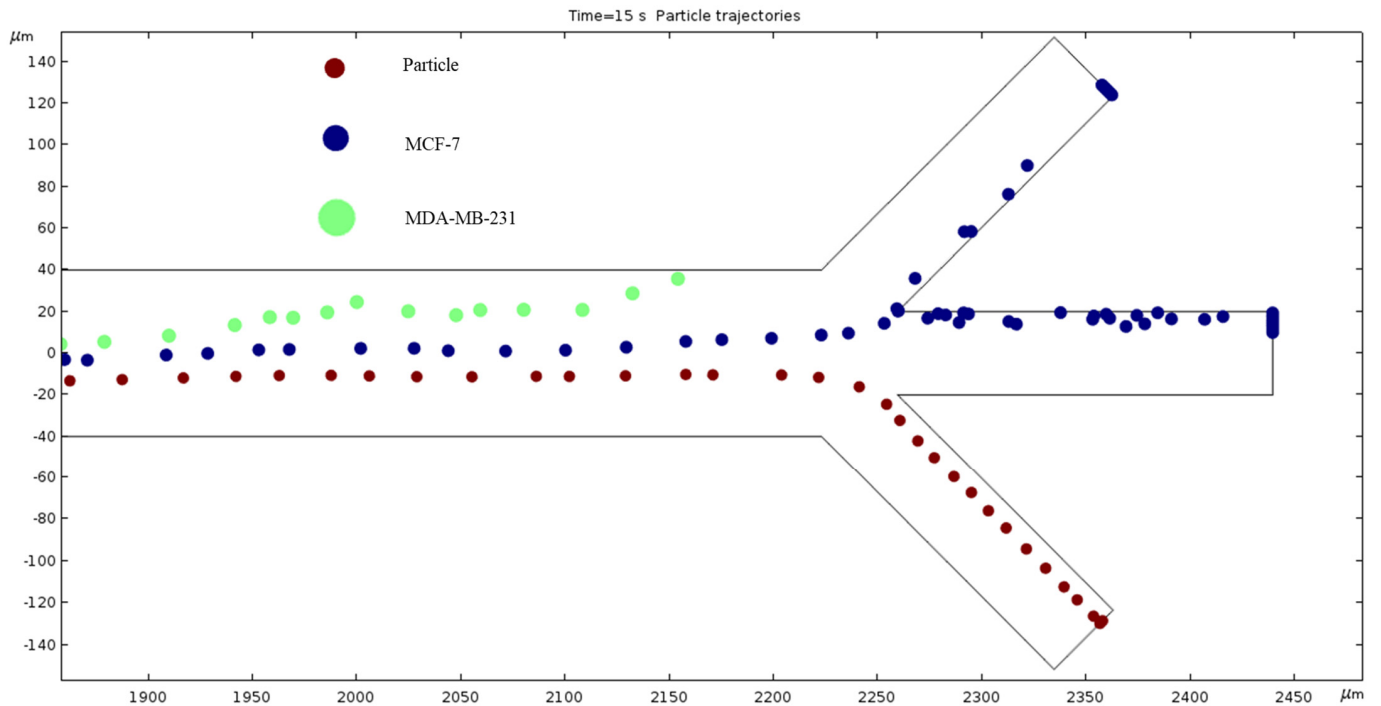
Figure 17. The depiction of our cell's trajectories at 1500 kHz AC through the electrodes.

Particle Trajectories (1800 kHz)—Figure 18 shows particles and cells trajectories inside the microchannel at 1800 kHz. At 1800 kHz AC, the trend of a counterclockwise bend continues, the MCF 7 cells exit through the top outlet, and the particles cells still exit through the bottom channel. At this point, we can further deduce that the MDA-MB-231 cells seem to have the most change in trajectory with the change in frequency. The MCF 7 cells change slightly less, and the particles cells are the most stubborn to change from the different materials.
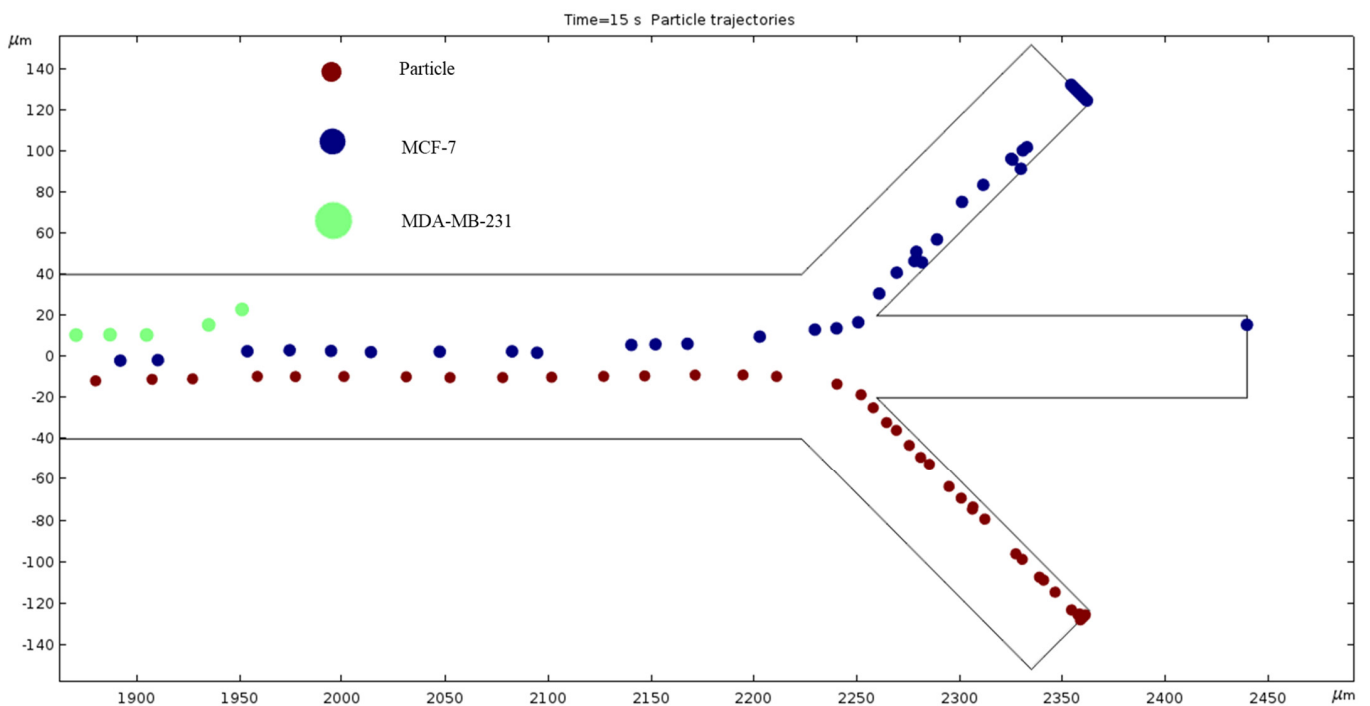

Figure 18. The diagram of cell trajectories when the frequency of AC is 1800 kHz.

Particle Trajectories (2200 kHz)—Figure 19 shows particles and cells trajectories inside the microchannel at 2200 kHz. Further increasing the frequency of AC to 2200 kHz, the particles finally reach the boundary to change their exit from the bottom channel to the middle channel. Like the MDA-MB-231 cells in Figure 18 and the MCF 7 cells in Figure 17, some particles still exit through the bottom outlet while the others exit through the middle outlet. The MDA-MB-231 and MCF 7 cells continue to bend upward. The positive dielectrophoresis forces attract the cells/particle toward the electrodes due to electric potential difference. The MDA-MB-231 cells are experiencing positive dielectrophoresis forces and the permittivity of the cells higher than the permittivity of the medium. Hence, at 2200 kHz, the MDA-MB-231 cells are trapped at the edge of the bottom electrode.
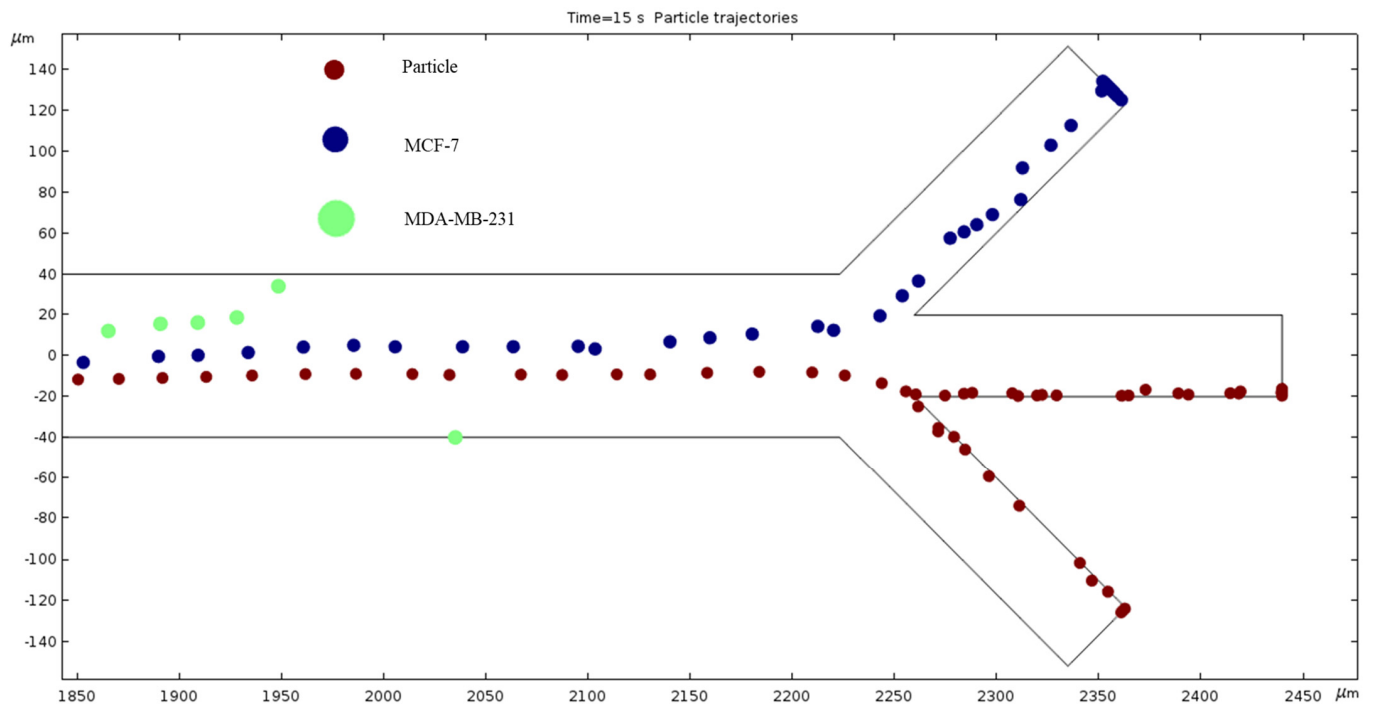

Figure 19. The electric field affects the particles shown in this diagram in a unique way when the frequency is 2200 kHz.

Particle Trajectories (4000 kHz)—Figure 20 shows particles and cells trajectories inside the microchannel at 4000 kHz. The frequency of AC through our microchannel's electrodes is set to 4000 kHz, and the particle velocities are recorded. Figure 20 shows the cells continuing the upward trend. However, the magnitude of this change seems to be decreasing because an increase of 1800 kHz does not reveal as much change as when comparing Figures 16 and 17, which is a 300 kHz difference in frequency. Particles are separated in the middle outlet and MCF 7 cells leave to exit in the top outlet.

Particle Trajectories (100,000 kHz)—Figure 21 shows particles and cells trajectories inside the microchannel at 100,000 kHz. When the frequency is increased 10-fold, our particle trajectories have returned to a similar motion path to when we started. In other words, Figures 13 and 21 look very similar, and we can expect those frequencies to produce the same results.
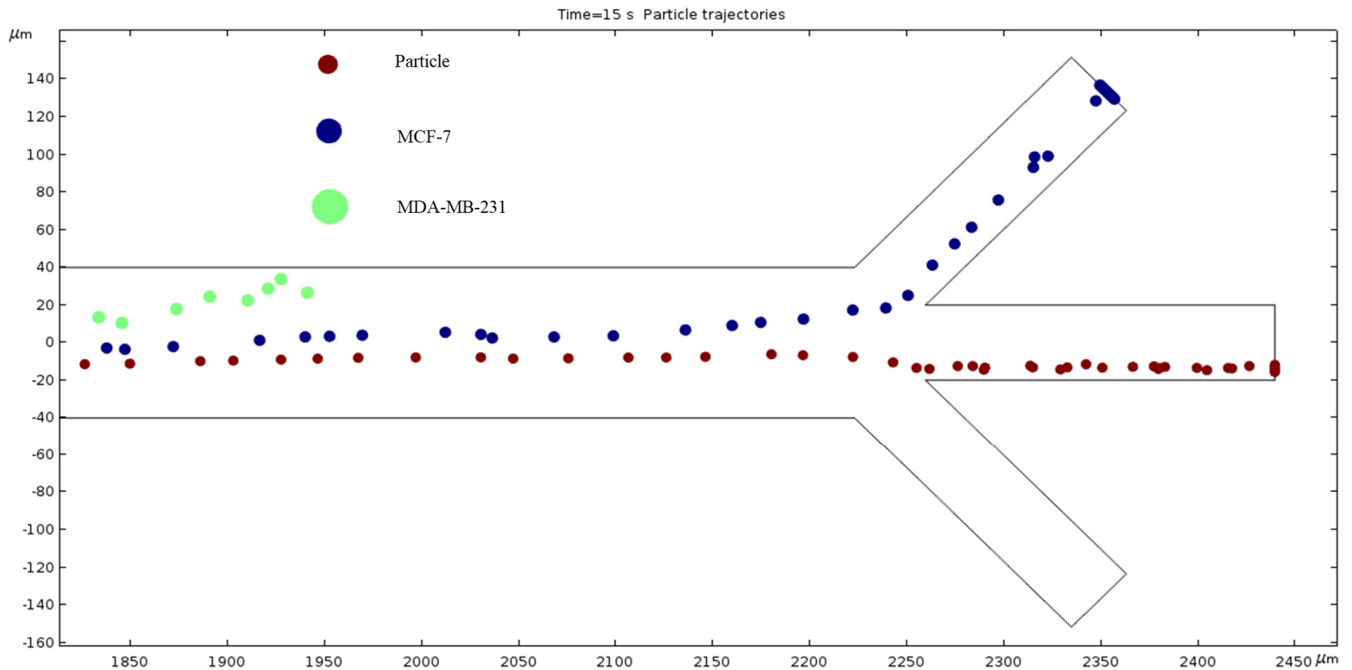
Figure 20. A depiction of the particle trajectories when the AC through the electrodes is 4000 kHz.
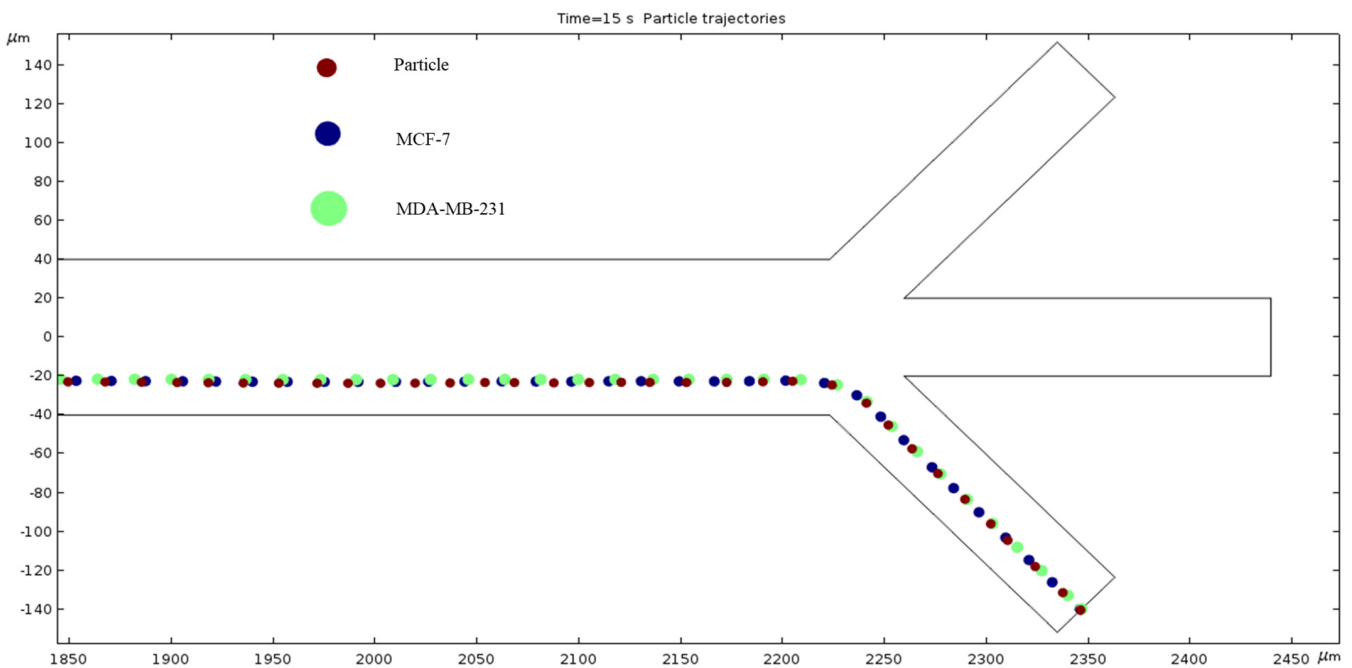
Figure 21. The diagram of our particles' path of motion when the frequency of electric field is 100,000 kHz.

Table 2 shows particles and cells are separated in different outlets in the microchannel. There are 16 electrodes used in the micro channel. The applied voltages are 1 V at the top electrodes and −2 V at the bottom electrodes. The numerical results are summarized in Table 2. Cells and particles are separated into different outlets due to dielectrophoresis (DEP).

Table 2. Cells are separated into different outlets at different applied frequencies.

Frequency	Separation in Outlet		
	Bottom	**Middle**	**Top**
10 KHz	Particles, MCF7, MDA-MB-231		
100 KHz	Particles, MCF7, MDA-MB-231		
800 KHz	Particles	MCF7, MDA-MB-231	
1000 KHz	Particles	MCF7, MDA-MB-231	MDA-MB-231
1200 KHz	Particles	MCF7	MDA-MB-231
1500 KHz	Particles	MCF7	MCF7
2000 KHz	Particles		MCF7
3000 KHz		Particles	MCF7
5000 KHz		Particles	MCF7
10,000 KHz	Particles	MCF7	
100,000 KHz	Particles, MCF7, MDA-MB-231		

4. Discussion

In order to fully grasp the intricacies of microfluidic devices used to transport biological molecules, it is crucial to examine the principles of dielectrophoresis (DEP) and the Clausius–Mossotti factor. DEP, as explained in detail by Doh and Cho (2005), involves the interaction between the dipole moment of neutral particles and non-uniform electric fields, allowing for the precise manipulation of particles in fluid environments [28]. This process is precious in microfluidic devices, enabling tasks such as trapping, translation, and the focusing of biological analytes. Additionally, as Farasat et al. (2022) highlighted, the Clausius–Mossotti factor plays a pivotal role in determining the direction and magnitude of DEP forces applied to particles [29]. Understanding these fundamental concepts is essential for optimizing the design and functionality of microfluidic devices, particularly in biomedical applications where the precise control over particle movement is crucial for effective separation and characterization processes.

Incorporating optimal parameters into the design of microfluidic devices for handling biological material is critical in maximizing device performance and efficacy. Doh and Cho (2005) discuss the application of hydrodynamic dielectrophoresis in continuous cell separation, emphasizing the significance of accurate control over cell movement within microchannels [28]. Advanced valve-controlled systems for the simultaneous separation of positive and negative DEP cells can significantly improve throughput and efficiency [28,29]. Research in this area highlights the importance of electrode design, fluid flow control, and automation in optimizing microfluidic device performance for handling biological samples. Our simulation adds to the research towards this goal.

Upon analyzing the simulated device design, it has been determined that the microchannel consists of 16 electrodes, with 8 pairs in total. The anodes are situated at the channel's top, while the cathodes are located at the bottom. All electrodes on the device are axisymmetric, with applied voltages of 1 V in the anodes and −2 V in the cathodes. The cathode's largest electrode size is 200 microns, while the anodes measure 50 microns. Figure 3 depicts the microchannel's surface potential, while Figure 4 illustrates the fluid flow with 0 nm/s inlet velocity. The maximum velocity recorded in this condition is 137.63 nm/s, with vortexes created between the anode and cathode due to the ACEO phenomenon, as seen at the end of the channel. When the pressure-driven flow is applied, a sinusoidal fluid flow pattern emerges and the maximum fluid velocity observed is 187.31 nm/s with 50 nm/s inlet velocity, as seen in Figure 5. As expected, with increased inlet velocity, the maximum fluid velocity also rises, as shown in Figure 6, where a clear sign wave and maximum 218.67 nm/s fluid velocity inside the channel are measured with

100 nm/s inlet velocity. Furthermore, a significant sign wave is observed in the last trial when the inlet velocity is 200 nm/s, as seen in Figure 7, where the maximum velocity reaches 300.05 nm/s. This increase in pressure-driven flow leads to a rise in the maximum fluid velocity due to the ACEO phenomenon.

In the graphs displayed in Figure 8, the maximum fluid velocity vs. time is illustrated at various frequencies. The data show a linear relationship between fluid velocity and time at 10 Hz, where as time increased, fluid velocity also increased. At the 15 s mark, the velocity of the fluid was measured at 40.31 nm/s. This same trend was observed at 100 Hz, where the maximum fluid velocity was 148.98 nm/s. However, 1000 Hz and 10,000 Hz produce different results. In both cases, fluid velocity increases from 0 to 10 s, but the trends show the opposite from 10 to 15 s. Figure 9 depicts a velocity vs. time graph that shows a constant horizontal line at 10,000 Hz. At 100 Hz, the maximum fluid velocity displays a sinusoidal pattern. At a low frequency (10 Hz), the maximum fluid velocity was measured at 202.11 nm/s at 10 s. Figure 10 shows no change in velocity vs. time graph for 100 Hz and 10,000 Hz cases. They showed the same trend as at 10 Hz and 1000 Hz, where their maximum fluid velocity was 100 nm/s. Figure 11 displays the same velocity vs. the time graph at 10, 1000, and 10,000 Hz. The only change observed is at 100 Hz, where the maximum velocity was 211.38 nm/s at 10 s. It is worth noting that the ACEO phenomenon can be observed in Figures 8–11.

To provide an overview, the microfluidic device is designed with a microchannel featuring three inlets and outlets, alongside eight pairs of electrodes on the side walls. The process involves injecting particles and cell mixtures at the bottom inlet, with fluid injection occurring at the middle and top inlets. Asymmetrically placed electrodes facilitate the creation of a non-uniform electric field, which is generated via the application of an AC electric field to the electrodes, resulting in DEP forces. Our study found that a positive DEP force is observed when the electrical polarization of particles and cells is higher than that of the surrounding medium, leading to their attraction. Conversely, an opposing DEP force occurs when the electrical polarization of particles and cells is lower than medium, resulting in their repulsion. Ultimately, the use of positive and negative DEP forces transport particles and cells in different directions, enabling their separation through the dielectrophoretic method.

The numerical results depicted in Figures 13–21 showcase the behavior of cells and particles under varying frequencies. At 100 kHz, all particles and cells underwent linear translation and were repelled towards the bottom outlet by negative DEP. At 800 kHz, the particles moved towards the bottom outlet while the MCF 7 and MDA-MB-231 cells were separated in the middle outlet (Figure 14). The MDA-MB-231 cells experienced DEP at 1000 kHz (Figure 15), while at the 1200 kHz frequency, particles, MCF 7, and MDA-MB-231 cells were successfully separated (Figure 16). At 1500 kHz, the MDA-MB-231 cells exhibited rotational movement, while the MCF 7 cells underwent negative DEP force (Figure 17). At 2200 kHz, particles and MCF 7 cells experienced a negative DEP force, and the MDA-MB-231 cells rotated counterclockwise and they experienced a positive DEP force (Figure 19). At 4000 kHz, the particles and MCF 7 cells were directed towards the middle and top outlets, respectively, while the MDA-MB-231 cells remained in the microchannel. When the frequency was increased to 100 MHz, all the particles and cells were expelled from the bottom outlet due to negative DEP. The ultimate objective of this project was to effectively separate particles and cells, which was accomplished through the application of various frequencies.

We measured cell and particle separation in microfluidics devices by changing the frequency range from 10 kHz to 100,000 kHz. The cell size, conductivity and permittivity are given in Table 1. The dielectrophoresis force depends on particle size. The results from the simulations revealed that the ACEO phenomenon plays an almost inconsequential role for cell and particle separations due to the very high frequency applied to electrodes. In this work, there are two forces acting on the cells and particles: one is the horizontal force, and another one is the vertical force. The horizontal force plays an important role when

the hydrodynamics and dielectrophoresis forces work on cells/particles. For review, the dielectrophoresis force acts on cells when cells move in a vertical direction. At 100 kHz, the hydrodynamics and dielectrophoresis forces work both cells and particles as they separate at the bottom of the outlet. Both cells separated in the middle outlet, due to the permittivity difference between the cells and medium at 800 kHz; in this condition, both cells also experience more dielectrophoresis force than particles. When 1200 kHz is applied at electrodes, the MDA-MB-231 cells separate to the top outlet, the MCF-7 cells separated to the middle outlet and the particles go through the bottom outlet. In this case, both MDA-MB-231 and MCF-7 cells experience negative dielectrophoresis force due to permittivity of the medium being higher than the permittivity of cells.

Previous research and simulations confirm the efficacy of ACEO in microfluidics. Analytical results indicate that as the inlet velocity increases, the net velocity also increases. Our simulations validate this prediction. However, we observed a phenomenon at high frequencies when attempting to determine the frequency at which our three distinct cells separate. The results indicate that 1200 kHz is the optimal frequency that enables each cell type to exit through their designated outlets. At low frequencies (0.01–500 kHz), our cells exhibit minimal separation and exit through the bottom outlet. When the frequency reaches 1000 kHz, our simulation reveals that the AC affects the particles differently, which is critical for the separation process.

Moreover, our observations indicate that particle trajectory alteration does have a limit beyond which any increase in frequency yields minimal impact on particle trajectory. We discovered that subjecting the electrodes to 100,000 kHz of AC successfully reverted the particle trajectories to their original path of motion, after starting with low frequencies of EF. Additionally, our findings suggest that achieving particle separation is predominantly reliant on frequency rather than inlet velocity. Our simulation revealed a consistent trend of inlet velocity being directly proportional to net velocity, while holding the frequency of EF constant.

Ongoing research efforts are constantly refining microfluidic device designs to meet the changing demands of biomedical applications. The integration of novel technologies from multiple fields is necessary to push the boundaries of microfluidic device functionality and utility. While microfluidic devices are already frequently used for high-throughput screening and analysis, their small sample volumes can lead to issues with sample heterogeneity and accuracy. To address this issue, further research is needed to scale up these devices to handle larger sample volumes while maintaining high levels of precision and accuracy. Further, the construction of a physical device to validate this simulation work would be a meaningful step. Collaborating closely with experts in biology, chemistry, and engineering is essential to the development of microfluidic devices that are optimized for their intended applications. Interdisciplinary collaboration is critical to the continued advancement of microfluidics technology and the potential for groundbreaking discoveries in the field of biomedical research.

5. Conclusions

ACEO has an effective reach, not only in mixing and moving fluids, but also in separating them. We showed that particles can be filtered in a specific range of frequencies using ACEO. This separation depends on the material of the particles and pressure-driven flow. COMSOL offers quick numerical simulations to allow us to pinpoint the most effective frequency and inlet velocity to allow for this particle separation. In conclusion, using the dielectrophoretic method, the microfluidics device with eight pairs of electrodes showed promising results in separating particles and cells. The AC electric field generated using the electrodes created positive and negative DEP forces, which attracted or repelled particles and cells, separating them. The simulation results showed that the frequency of the AC electric field played a crucial role in the separation process. The ACEO phenomenon was also observed, which increased the fluid velocity and vortexes inside the microchannel. The simulation results agreed with the analytical results, which predicted an increase in

net velocity with the increase in inlet velocity. This research provides a foundation for developing microfluidic devices for various applications, such as cell sorting, drug delivery, and biosensors. The dielectrophoretic method offers a non-invasive way to manipulate particles and cells, which is crucial in biological and medical applications.

Further research can focus on optimizing the microfluidic device design, electrode placement, and frequency to improve the separation efficiency. Additionally, the study can be extended to investigate the effects of different particle and cell types, sizes, and concentrations on the separation process. Overall, this research demonstrates the potential of microfluidics and dielectrophoresis in advancing biomedical research and applications.

References

1. Karniadakis, G.; Beskok, A.; Aluru, N. *Microflows and Nanoflows: Fundamentals and Simulation*; Springer Science & Business Media: Berlin/Heidelberg, Germany, 2006; Volume 29.
2. Hsu, W.-L.; Daiguji, H. Manipulation of Protein Translocation through Nanopores by Flow Field Control and Application to Nanopore Sensors. *Anal. Chem.* **2016**, *88*, 9251–9258. [CrossRef]
3. Chen, X.; Zhang, S.; Zhang, L.; Yao, Z.; Chen, X.; Zheng, Y.; Liu, Y. Applications and theory of electrokinetic enrichment in micro-nanofluidic chips. *Biomed. Microdevices* **2017**, *19*, 19. [CrossRef] [PubMed]
4. Mondal, K.; Ali, M.A.; Srivastava, S.; Malhotra, B.D.; Sharma, A. Electrospun functional micro/nanochannels embedded in porous carbon electrodes for microfluidic biosensing. *Sens. Actuators B Chem.* **2016**, *229*, 82–91. [CrossRef]
5. Matteucci, M.; Heiskanen, A.; Zór, K.; Emnéus, J.; Taboryski, R. Comparison of ultrasonic welding and thermal bonding for the integration of thin film metal electrodes in injection molded polymeric lab-on-chip systems for electrochemistry. *Sensors* **2016**, *16*, 1795. [CrossRef] [PubMed]
6. Hsieh, T.C.; Wijeratne, E.K.; Liang, J.Y.; Gunatilaka, A.L.; Wu, J.M. Differential control of growth, cell cycle progression, and expression of NF-κB in human breast cancer cells MCF-7, MCF-10A, and MDA-MB-231 by ponicidin and oridonin, diterpenoids from the chinese herb Rabdosia rubescens. *Biochem. Biophys. Res. Commun.* **2005**, *337*, 224–231. [CrossRef] [PubMed]
7. Moses, S.L.; Edwards, V.M.; Brantley, E. Cytotoxicity in MCF-7 and MDA-MB-231 breast cancer cells, without harming MCF-10A healthy cells. *J. Nanomed. Nanotechnol.* **2016**, *7*, 1–11.
8. Isfahani, A.M.; Tasdighi, I.; Karimipour, A.; Shirani, E.; Afrand, M. A joint lattice Boltzmann and molecular dynamics investigation for thermohydraulical simulation of nano flows through porous media. *Eur. J. Mech.-B/Fluids* **2016**, *55*, 15–23. [CrossRef]
9. Meghdadi Isfahani, A.H. Parametric study of rarefaction effects on micro-and nanoscale thermal flows in porous structures. *J. Heat Transf.* **2017**, *139*, 092601. [CrossRef]
10. Bagi, M.; Amjad, F.; Ghoreishian, S.M.; Sohrabi Shahsavari, S.; Huh, Y.S.; Moraveji, M.K.; Shimpalee, S. Advances in technical assessment of spiral inertial microfluidic devices toward bioparticle separation and profiling: A critical review. *BioChip J.* **2024**, *18*, 1–23. [CrossRef]
11. Hettiarachchi, S.; Cha, H.; Ouyang, L.; Mudugamuwa, A.; An, H.; Kijanka, G.; Kashaninejad, N.; Nguyen, N.-T.; Zhang, J. Recent microfluidic advances in submicron to nanoparticle manipulation and separation. *Lab Chip* **2023**, *23*, 982–1010. [CrossRef]
12. Dutta, D.; Smith, K.; Palmer, X. Long-Range ACEO Phenomena in Microfluidic Channel. *Surfaces* **2023**, *6*, 145–163. [CrossRef]
13. Suh, Y.K.; Kang, S. A Review on Mixing in Microfluidics. *Micromachines* **2010**, *1*, 82–111. [CrossRef]
14. Chang, C.-C.; Yang, R.-J. Electrokinetic mixing in microfluidic systems. *Microfluid. Nanofluid.* **2007**, *3*, 501–525. [CrossRef]
15. Rashidi, S.; Bafekr, H.; Valipour, M.S.; Esfahani, J.A. A review on the application, simulation, and experiment of the electrokinetic mixers. *Chem. Eng. Process. Process. Intensif.* **2018**, *126*, 108–122. [CrossRef]
16. Johnson, T.J.; Ross, A.D.; Locascio, L.E. Rapid Microfluidic Mixing. *Anal. Chem.* **2002**, *74*, 45–51. [CrossRef] [PubMed]

17. Glasgow, I.; Aubry, N. Enhancement of microfluidic mixing using time pulsing. *Lab Chip* **2003**, *3*, 114–120. [CrossRef] [PubMed]
18. Shang, X.; Huang, X.; Yang, C. Vortex generation and control in a microfluidic chamber with actuations. *Phys. Fluids* **2016**, *28*, 122001. [CrossRef]
19. Daghighi, Y.; Li, D. Numerical study of a novel induced-charge electrokinetic micro-mixer. *Anal. Chim. Acta* **2013**, *763*, 28–37. [CrossRef] [PubMed]
20. Qian, S.; Bau, H.H. Magneto-hydrodynamics based microfluidics. *Mech. Res. Commun.* **2009**, *36*, 10–21. [CrossRef]
21. Cai, G.; Xue, L.; Zhang, H.; Lin, J. A Review on Micromixers. *Micromachines* **2017**, *8*, 274. [CrossRef]
22. Sigdel, I.; Gupta, N.; Faizee, F.; Khare, V.M.; Tiwari, A.K.; Tang, Y. Biomimetic microfluidic platforms for the assessment of breast cancer metastasis. *Front. Bioeng. Biotechnol.* **2021**, *9*, 633671. [CrossRef] [PubMed]
23. Dutta, D.; Palmer, X.L.; Ortega-Rodas, J.; Balraj, V.; Dastider, I.G.; Chandra, S. Biomechanical and Biophysical Properties of Breast Cancer cells under varying glycemic regimens. *Breast Cancer Basic Clin. Res.* **2020**, *14*, 1178223420972362. [CrossRef] [PubMed]
24. Dutta, D.; Russell, C.; Kim, J.; Chandra, S. Differential mobility of breast cancer cells and normal breast epithelial cells under DC electrophoresis and electroosmosis. *Anticancer Res.* **2018**, *38*, 5733–5738. [CrossRef] [PubMed]
25. Jubery, T.Z.; Dutta, P. A fast algorithm to predict cell trajectories in microdevices using dielectrophoresis. *Numer. Heat Transf. Part A Appl.* **2013**, *64*, 107–131. [CrossRef]
26. Shirmohammadli, V.; Manavizadeh, N. Numerical modeling of cell trajectory inside a dielectrophoresis microdevice designed for breast cancer cell screening. *IEEE Sens. J.* **2018**, *18*, 8215–8222. [CrossRef]
27. DM Campos, C.; Uning, K.T.; Barmuta, P.; Markovic, T.; Yadav, R.; Mangraviti, G.; Ocket, I.; Van Roy, W.; Lagae, L.; Liu, C. Use of high frequency electrorotation to identify cytoplasmic changes in cells non-disruptively. *Biomed. Microdevices* **2023**, *25*, 39. [CrossRef] [PubMed]
28. Doh, I.; Cho, Y.H. A continuous cell separation chip using hydrodynamic dielectrophoresis (DEP) process. *Sens. Actuators A Phys.* **2005**, *121*, 59–65. [CrossRef]
29. Farasat, M.; Aalaei, E.; Kheirati Ronizi, S.; Bakhshi, A.; Mirhosseini, S.; Zhang, J.; Nguyen, N.-T.; Kashaninejad, N. Signal-Based Methods in Dielectrophoresis for Cell and Particle Separation. *Biosensors* **2022**, *12*, 510. [CrossRef]
30. Huang, Y.; Holzel, R.; Pethig, R.; Wang, X.B. Differences in the AC electrodynamics of viable and non-viable yeast cells determined through combined dielectrophoresis and electrorotation studies. *Phys. Med. Biol.* **1992**, *37*, 1499. [CrossRef] [PubMed]
31. Mei, L.; Cui, D.; Shen, J.; Dutta, D.; Brown, W.; Zhang, L.; Dabipi, I.K. Electroosmotic mixing of non-newtonian fluid in a microchannel with obstacles and zeta potential heterogeneity. *Micromachines* **2021**, *12*, 431. [CrossRef]
32. TruongVo, T.N.; Kennedy, R.M.; Chen, H.; Chen, A.; Berndt, A.; Agarwal, M.; Zhu, L.; Nakshatri, H.; Wallace, J.; Na, S.; et al. Microfluidic channel for characterizing normal and breast cancer cells. *J. Micromech. Microeng.* **2017**, *27*, 035017. [CrossRef]